RAPID RECONFIGURATION DIRECT SPACE-TO-TIME PULSE SHAPING USING A HIGH SPEED ASYMMETRIC FABRY-PEROT QUANTUM WELL MODULATOR ARRAY

A Dissertation
Submitted to the Faculty
of
Purdue University
by
Albert Vega

In Partial Fulfillment of the
Requirements for the Degree
of
Doctor of Philosophy

May 2010
Purdue University
West Lafayette, Indiana

TABLE OF CONTENTS

Page

LIST OF TABLES iv

LIST OF FIGURES v

ABSTRACT ix

1 INTRODUCTION 1

2 MODULATOR BACKGROUND 4

2.1 Fabry-Perot Cavity 4

2.2 Absorbing Material and Quantum Confinement 8

2.3 Stark Shift 12

2.4 Exciton 13

3 DEVICE FABRICATION AND DC TESTING 15

3.1 Wafer Growth, Measurement, and Preparation 15

3.2 P-ohmic Contacts 17

3.3 Mesa Etch 17

3.4 N-ohmic Contacts and I-V testing 19

3.5 Coplanar Waveguide and Biased Spectral Measurements 21

3.6 Rear Mirror 27

3.7 Anti-Reflective Coating 33

3.8 DC Spectral Extinction Ratio 39

4 RF DEVICE PERFORMANCE 41

5 DST PULSE SHAPING WITH DEVICE ARRAY 45

5.1 DST pulse shaping with modified Arrayed Waveguide Grating . . . 45

5.2 Static DST pulse shaping with array of modulators 48

5.3 Rapid update DST pulse shaping 52

6 CONCLUSIONS AND FUTURE WORK 59

Page

6.1 Conslusions 59
6.2 Device Improvement 59
    6.2.1 New Device Material 59
    6.2.2 Heating 61
    6.2.3 Capacitance 62
6.3 Multi-Device Functionality 63
LIST OF REFERENCES 66
A DEVICE SIMULATIONS 69
VITA 74

LIST OF TABLES

Table Page

4.1 AC testing of various devices 43

6.1 Current device areas and cutoff frequencies compared with possible reduced area devices and estimated cutoff frequencies. 63

LIST OF FIGURES

Figure Page

1.1 Fourier Transform pulse shaper 1

1.2 Direct Space-to-Time pulse shaper 2

1.3 Integrated DST pulse shaper using AWG and fixed spatial pattern . . . 2

2.1 Fabry-Perot Cavity 4

2.2 Transmission of symmetric FP cavity with $R_F=R_B=30\%$ 5

2.3 Transmission of asymmetric FP cavity with $R_F=30\%$ and $R_B=90\%$ . . 6

2.4 Reflection of symmetric and asymmetric FP cavity 7

2.5 Reflection of FP cavity with $R_F=30\%$ and R_B varying from 30% to 99% 7

2.6 Energy band diagram and absorption event 8

2.7 Example absorption curve 9

2.8 Infinite barrier quantum well, energy levels, and probability density functions 9

2.9 Finite barrier quantum well, energy levels, and probability density functions 10

2.10 Quantum well and minimum energy absorbed 11

2.11 Example absorption curve in relation to range of interest 12

2.12 Example of shifting absorption 12

2.13 Quantum well under electric field and reduced minimum energy absorbed 13

2.14 Examples of absorption with exciton peak for different voltages 14

3.1 Wafer growth table 15

3.2 Wafer spectral measurement setup 16

3.3 Light interacting with the wafer 16

3.4 Overview of device processing mask 17

3.5 P-ohmic contact step, top down view 18

Figure Page

3.6 P-ohmic contact step, profile view 18
3.7 Mesa etch step, top down view 19
3.8 Mesa etch step, profile view 19
3.9 N-ohmic contact step, top down view 20
3.10 N-ohmic contact step, profile view 20
3.11 N-ohmic I-V plots 20
3.12 P-ohmic I-V plots 20
3.13 Device I-V curve 21
3.14 Close view of reverse bias current 21
3.15 Top down view of waveguide step 22
3.16 Device spectral measurement setup 23
3.17 Light interaction and applied bias upon device 23
3.18 Device absorption for varying applied voltages 23
3.19 Device absorption difference for varying voltages 23
3.20 Profile view of tuning etch step 25
3.21 Flow chart of the tuning etch process 25
3.22 Device simulation after etching, no bias 26
3.23 Device measurement after etching, no bias 26
3.24 Device simulation after etching, -10V bias 27
3.25 Device measurement after etching, -10V bias 27
3.26 Mirror step, top-down view 28
3.27 Mirror step, profile view 28
3.28 Device measurement after back mirror, no bias 29
3.29 Device measurement after back mirror, -10V bias 29
3.30 Reflection difference of the device after back mirror 30
3.31 Simulated desired response of device with mirror, no bias 30
3.32 Simulated desired response of device with mirror, -10V bias 30
3.33 Spectral characteristics of titanium/gold mirror on InP 31

Figure Page

3.34 Spectral characteristics of gold mirror on InP 31
3.35 Spectral characteristics of gold mirror on InAlAs 32
3.36 Selected devices for varying etch test. 33
3.37 Data from device with back mirror under -10V bias 33
3.38 Simulation of device with mirror under -10V bias 33
3.39 Reflectivity of first attempt of AR on InP. 36
3.40 Reflectivity of first attempt of AR on InP along with simulated data. . 36
3.41 Reflectivity of second attempt of AR on InP. 37
3.42 Reflectivity of second attempt of AR in InP along with simulated data. 37
3.43 Spectral data from device with back mirror and AR coating with zero bias 38
3.44 Spectral data from device with back mirror and AR coating with -5V bias 38
3.45 Spectral data from device with back mirror and AR coating with -10V bias 38
3.46 Spectral data from device with back mirror and AR coating with -15V bias 38
3.47 Device reflectivity as bias is changed. 39
3.48 Extinction ratio of device between zero bias and -15V bias. 40
3.49 Comparison of extinction ratios between 0V to -15V and -5V to -15V. . 40
4.1 Setup for testing high speed performance of the device. 41
4.2 250 μm device under AC testing while varying drive frequency 42
4.3 AC response of 250μm device as a function of frequency. 43
4.4 Plot of cutoff frequencies for devices along with curve fitting the data points. 44
5.1 Typical AWG 45
5.2 An output pulse train generated by an AWG. 47
5.3 An output pulse train generated by double passing through a modified AWG. 47
5.4 An output pulse train generated by an AWG. 48
5.5 AWG with telescope to match used guides with array of devices. 49

Figure Page

5.6 Setup for testing DST pulse shaping at DC rates. Components: actively mode-locked laser (AML), dispersion compensating fiber (DCF), erbium doped fiber amplifier (EDFA), polarization controller (PC), polarizer (Pol), cross correlation (XCORR). 49

5.7 Output pulse trains under different biases. 51

5.8 Output pulse trains with different devices under DC bias to show diversity of control. 52

5.9 Setup for DST pulse shaping at RF rates. Components: actively mode-locked laser (AML), photodiode (PD), dispersion compensating fiber (DCF), erbium doped fiber amplifier (EDFA), polarization controller (PC), polarizer (Pol), cross correlation (XCORR), intensity modulator (IM), and bit error rate tester (BERT). 53

5.10 High speed device drive signal. 55

5.11 Various AWG output pulse trains due to varying device drive signal. . 55

5.12 Evolution of output pulse train as RF delay is swept through π range for 500MHz. 56

5.13 Examples of high speed switching between "on/off" states for two devices. 57

5.14 Evolution of output pulse train as RF delay is swept just over a π range for 1GHz. 58

6.1 Material structure for new device. 60

6.2 Current device structure with bottom side illumination. 60

6.3 New device structure with top side illumination. 60

6.4 Example of signal degradation when applying an RF signal. 61

6.5 Device area for current device (a) and new device (b). 63

6.6 Board with reducing transmission lines to drive more than one device. . 64

Appendix Figure

A.1 Simple transmission line 69

A.2 Simple interface of two films with load impedance 69

A.3 Transmission line approach to using an input impedance 71

A.4 Thin film approach to using an input impedance 71

ABSTRACT

Vega, Albert. Ph.D., Purdue University, May 2010. Rapid Reconfiguration Direct Space-to-Time Pulse Shaping Using a High Speed Asymmetric Fabry-Perot Quantum Well Modulator Array. Major Professor: Andrew M. Weiner.

Optical pulse shaping has been a useful tool for creating user defined optical waveforms for various applications. However, pulse shaping is often limited by fixed masks or the slow switching speeds of commonly used opto-electronic modulators used as spatial profiles within these experiments. These masks and modulators assist in performing the transformation of a short optical pulse into a desired waveform, but their properties do not change between input pulses when a high repetition rate input source is used. The ability to rapidly reconfigure the spatial profile within the pulse shaper would allow the possibility of shaping to occur on an input pulse-by-pulse basis. For our solution, we turn to the asymmetric Fabry-Perot quantum well modulator for its high-speed functionality and optical bandwidth capabilities. An array of such devices could provide a quickly changing spatial profile that would enable rapid reconfiguration. Device design, fabrication, and testing will be addressed along with pulse shaping experiments and results.

1. INTRODUCTION

Pulse shaping has proven itself very useful in the area of optics by providing user specified waveforms for a wide range of applications. Through the use of optical components and devices, a short burst of light can be transformed into a variety of waveforms. One common method of pulse shaping is the Fourier-transform (FT) pulse shaper. FT shaping is performed by manipulating the Fourier components of the input pulse. As light pulses get shorter, they contain more wavelengths of light or larger bandwidth. These individual wavelengths can be adjusted if they can be spatially separated [1]. Figure 1.1 shows a diagram of a FT pulse shaper. The input optical pulse has its different wavelengths spatially dispersed by a diffraction grating.

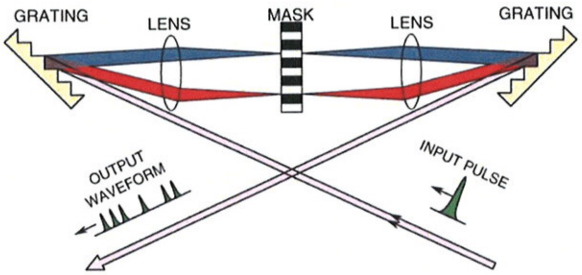

Fig. 1.1. Fourier Transform pulse shaper

A lens focuses the spectral components to a plane where a spatial light modulator (SLM) can change the amplitude, phase, or both amplitude and phase of the spectral components. The rest of the shaper re-combines the light into an output pulse with the desired amplitude and phase characteristics [2].

Another form of pulse shaping is the Direct Space-to-Time (DST) pulse shaper. This pulse shaper takes a short optical input pulse and maps the features of a spatial pattern onto the output pulse [3, 4]. Figure 1.2 shows an example of a DST pulse shaper using bulk optics. Another form of the DST pulse shaper is in integrated optics. Instead of using large objects such as lenses and a diffraction grating, the same functionality is provided in a much smaller space. A modified Arrayed Waveguide Grating (AWG) with a reflective spatial pattern on one end can provide the same effect as the bulk optics version, but with a much smaller footprint [5]. Figure 1.3 shows a figure of the integrated DST pulse shaper. Both pulse shapers allow the creation of a desired output waveform from a short input pulse, and both use a pattern or modulator at certain locations to achieve this effect. A fixed spatial mask can provide an amplitude pattern, or a liquid crystal modulator (LCM) can provide amplitude or phase modulation [6, 7]. The drawback from using either one of these is speed of changing the pattern. The fixed pattern must be changed by hand, and the LCM has a switching speed on the order of milliseconds. The input pulse to either system

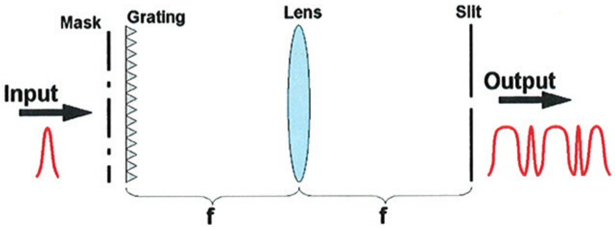

Fig. 1.2. Direct Space-to-Time pulse shaper

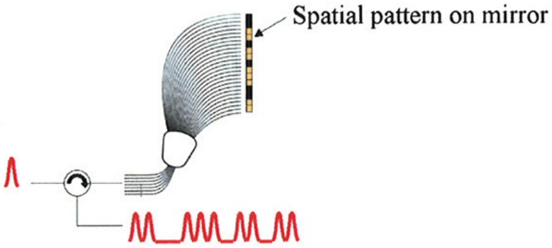

Fig. 1.3. Integrated DST pulse shaper using AWG and fixed spatial pattern

can be repeated $>10^9$ times a second (<1 nanosecond), and this would lead to many input pulses seeing the same pattern. A modulator with a very fast switching speed is required to rapidly update the spatial profile to generate specific output patterns with every new input pulse. Rapid update integrated DST pulse shaping has a possible application as a high-speed parallel-to-serial converter [8, 9], where multiple sources of relatively slow electrical data used to drive modulators would be serialized onto a onto a faster optical pulse train. To provide these rapid spatial updates, we turn to the Asymmetric Fabry-Perot Quantum Well Modulator. This device can provide good modulation, fast operation, and has reasonable optical bandwidth [10, 11], and a number of these modulators within an array could resemble a rapidly changing spatial profile. These devices are also easy to use within the above mentioned pulse shaping experiments due to surface normal operation, which does not require coupling of light into waveguides to perform its modulation.

Current efforts toward pulse shaper reconfiguration typically involves the usage of LCMs as spatial profiles. Slow LCM transition times have led to micro-electro-mechanical systems (MEMS) micromirror arrays being used for spatial patterning [12]. MEMS micromirrors have typical switching times in the range of milliseconds down to approximately microseconds [13–15], however the fastest devices have not been implemented within pulse shapers. Implementation of these devices could result in pulse shaper update rates of 4.4MHz (225ns). Further efforts at faster reconfiguration using beam steering over a two-dimensional LCM in an FT shaper has resulted in update rates of 140kHz (7.1us) [16]. Acousto-optic modulators used in FT shapers as a spatial profile has yielded a reconfiguration rate of 800kHz (1.25us) [17], but this is still not suitable for high repetition rate functionality. A GaAs integrated waveguide optical phased array has been able to provide waveform updating at a rate of 33MHz (30ns) [18] when implemented within an FT shaper. This document will discuss the background and use of a reflection modulator within a DST pulse shaper not only providing an increase of operating speed by greater than an order of magnitude, but while maintaining good performance at this speed.

2. MODULATOR BACKGROUND

2.1 Fabry-Perot Cavity

This section will break down the name of Asymmetric Fabry-Perot (AFP) Quantum Well (QW) Modulator and will lead to the explanation of the functionality of the device. The first step is to look at the portion "Asymmetric Fabry-Perot". A standard Fabry-Perot device is a cavity created by some type of medium between two reflectors or mirrors [19], as shown in Figure 2.1. This device is commonly used as an optical filter, allowing only certain frequencies which resonate within the cavity to pass through it. This type of operation is achieved by having the round trip cavity length be an integer multiple of the wavelength of the light. The transmission of the cavity is given by

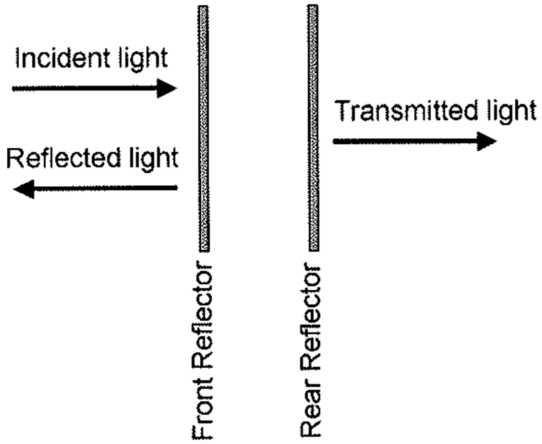

Fig. 2.1. Fabry-Perot Cavity

$$T(\theta) = \left\{ \frac{(1-R_F)(1-R_B)}{\left(1-\sqrt{R_F R_B}\right)^2 + 4\sqrt{R_F R_B} sin^2\theta} \right\} \tag{2.1}$$

where θ is the optical length of the cavity [20]. To relay this to a physical distance between reflectors,

$$\theta = \frac{2\pi n d}{\lambda} \tag{2.2}$$

where λ is the wavelength in the medium, d is the distance between the reflectors, and n is an integer. Figure 2.2 shows an example plot of what the transmission of the device would look like if many wavelengths were incident upon the cavity. This plot would be created by substituting equation (2.2) into equation (A.7) and varying the wavelength. The peaks indicate where the resonance occurs. The width of the peaks and the height can be adjusted by changing the values of the reflectors which create the cavity [20]. One can choose two reflectors with the same reflectivity (symmetric) or choose reflectors that are of different values (asymmetric). This reflector symmetry affects the height of the resonant peak. If the symmetric configuration is chosen, all of the power at the resonant wavelengths will be completely transmitted. Figure 2.2 shows and example of the symmetric configuration with R_F=R_B=30%. Note the height of the peaks. If we were to choose the asymmetric example, Figure 2.3 would show the transmission with the front reflector at 30% and the back at 90%. Again, note the height of the peaks. If one were to operate at or around the resonant wavelength, one could have an optical modulator if we could make a device that

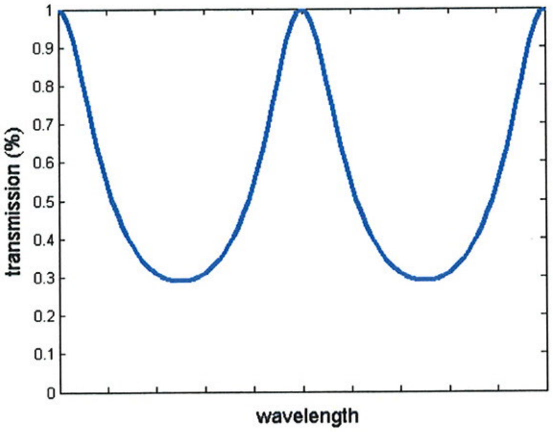

Fig. 2.2. Transmission of symmetric FP cavity with R_F=R_B=30%

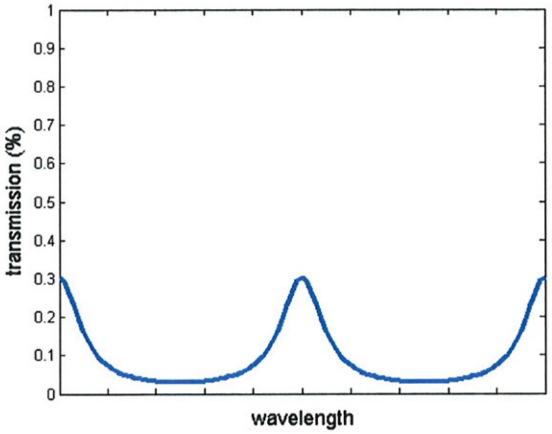

Fig. 2.3. Transmission of asymmetric FP cavity with R_F=30% and R_B=90%

could change (or effectively change) one of the reflectors. This device would be a transmission modulator and would be able to switch between an "on" state where all the light is transmitted and an "off" state where close to zero light is transmitted. Typically, the AFP modulator is operated in reflection mode, so one can also make a reflection modulator by looking at the reflected power from the above device. The reflected power is determined by R=1-T if there is no loss or absorption in the cavity. The only difference is that when the transmission modulator is "on", the reflection modulator is "off" when all the power is transmitted and none is reflected, and vice versa. Figure 2.4 shows an example of the reflected power for such a reflection modulator with both its "on/off" states. Not only can the device have binary reflective states, but the reflectivity can be varied between the states. Figure 2.5 shows the total cavity reflectivity as a function of fixed front reflector and varying back reflector. Now we have a possible way to create an optical modulator, the next step is to generate the effect of changing the reflectivity of the back mirror. Physically changing the actual reflectivity of the back mirror between states is impossible, but giving the appearance is not. The method to accomplish this is by inserting an absorber into the cavity [21]. When looking at the reflection of the device, inserting the absorber is a method of creating loss in the cavity which results in less light being reflected. When considering

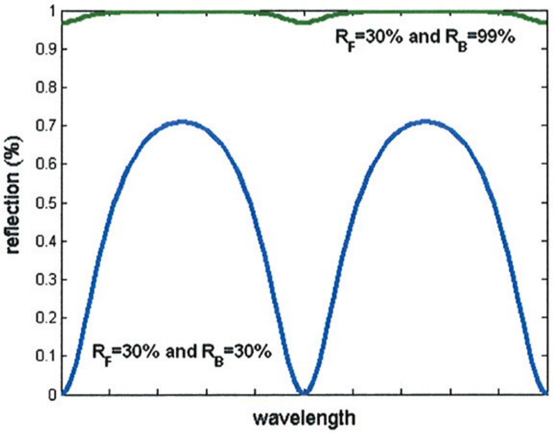

Fig. 2.4. Reflection of symmetric and asymmetric FP cavity

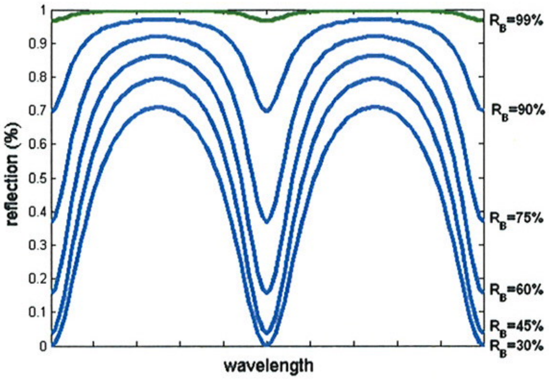

Fig. 2.5. Reflection of FP cavity with R_F=30% and R_B varying from 30% to 99%

the asymmetric Fabry-Perot, where R_F=30% and R_B=100%, the loss in the cavity gives the same effect as light escaping from the rear reflector. Light escaping from the rear reflector is equivalent to saying it has a lower reflectivity, or gives the same result as the insertion of an absorber [22].

2.2 Absorbing Material and Quantum Confinement

Next, we need to physically realize this absorbing material which will create the modulation effect of the device. In the "on" or highly reflective state of the device, the absorber needs to have little or no absorption. With the "off" or low reflectivity state of the device, the absorber must supply the correct amount absorption in order to produce the effect of a lower reflectivity of the rear reflector. The absorbing material is realized by use of quantum well material [23]. Typically, materials have an absorption edge related to the band gap, E_G, the difference between the conduction and valence bands of the material. Figure 2.6 shows the material band gap with the absorption of a photon causing an electron to be excited into the conduction band leaving behind a hole or an absence of an electron in the valence band. Also, an example of the absorption for different wavelengths is shown in Figure 2.7 for this material. This edge of the absorption plot is a function of the material, but creating quantum wells allows one to tailor the position of the absorption edge. This is accomplished by adjusting the height and width of the barrier material which separates the wells. In a quantum well, bottom of the well is not lowest energy level for a particle to exist. Since there is electron/hole confinement, the actual minimum energy level is higher than the bottom of the well [24]. Figure 2.8 shows this effect and also shows that the accepted energy levels in the well are quantized, not continuous. Given the case of a

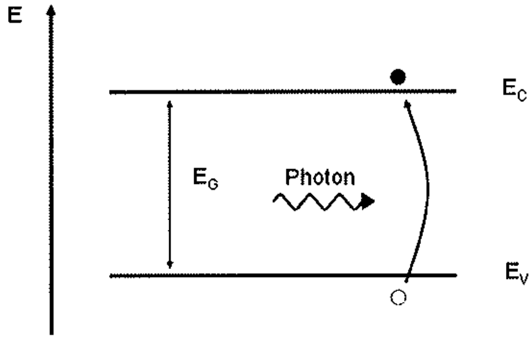

Fig. 2.6. Energy band diagram and absorption event

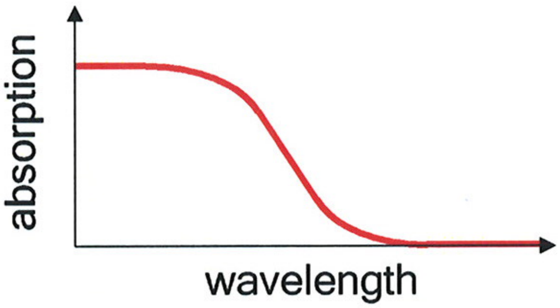

Fig. 2.7. Example absorption curve

quantum well with an infinite energy barrier, the energies allowed within the well are given by

$$E_n = \frac{n^2\pi^2\hbar^2}{2mL^2}, n = 1, 2, 3, ... \tag{2.3}$$

where m is the mass of the particle in the well, and L is the width of the well. The lowest energy is given when n=1. Figure 2.8 shows the first three energy levels for this case along with their probability density functions. Since the materials in the device design do not contain infinite energy barriers, the particle in the well is allowed to have a probability of existing in the barrier region, as shown in Figure 2.9. The displayed probability density function and associated wavefunction are longer in

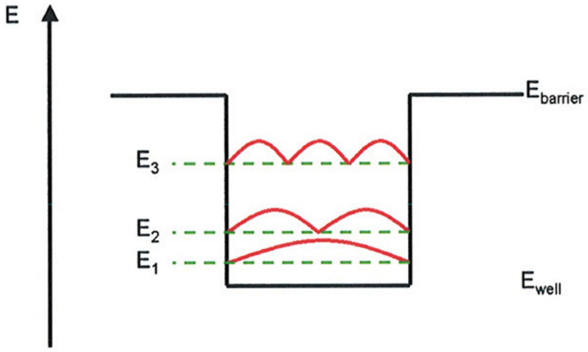

Fig. 2.8. Infinite barrier quantum well, energy levels, and probability density functions

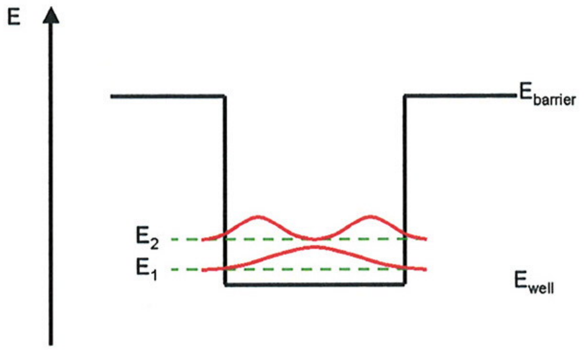

Fig. 2.9. Finite barrier quantum well, energy levels, and probability density functions

wavelength in comparison to the infinite quantum well shown previously, indicating lower energies for each quantized state. Still, the energy states are greater than that of the energy of the well and are not continuous. The lowest allowed energy state is determined by numerically solving

$$\xi tan\xi = \frac{m_{well}}{m_{barrier}}\sqrt{\frac{m_{barrier}E_0L^2}{2\hbar^2} - \frac{m_{barrier}}{m_{well}}\xi^2} \tag{2.4}$$

where

$$\xi = \sqrt{\frac{m_{well}EL^2}{2\hbar^2}} \tag{2.5}$$

and m_{well} is the effective mass of the particle in the well material, $m_{barrier}$ is the effective mass of the particle in the barrier material, L is the width of the well, and E_0 is the energy height of the barrier over that of the well [25]. Finding the lowest value of E in equation (2.4) gives the lowest energy state.

With bulk material, the largest wavelength absorbed has energy equal to the band gap of the material. However, within a quantum well, the lowest energy allowed to be absorbed is equal to the difference of the lowest allowed energy in the well for the conduction band, E_{C1}, and the lowest energy allowed in the well

$$E_1 = E_{C1} - E_{V1} \tag{2.6}$$

for the valence band, E_{V1}. This leads to an increase of the minimum energy photon absorbed over that of the bulk material. An example of this is shown in Figure 2.10. The absorption is now a function of the physical size of the quantum well, and

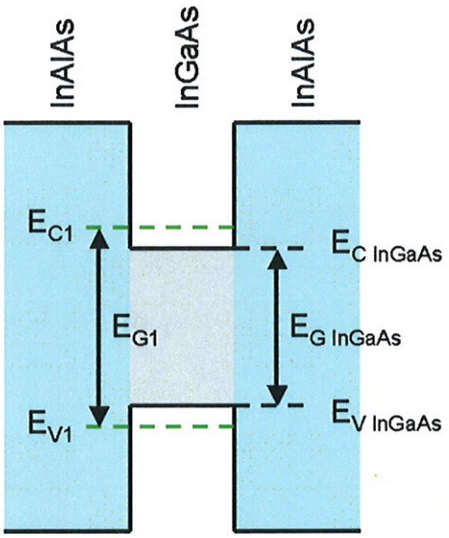

Fig. 2.10. Quantum well and minimum energy absorbed

this is useful because this allows the positioning of the absorption edge near to the wavelengths of interest that will be used in this device. Figure 2.11 shows an example of the absorption of the quantum well material in reference to the wavelengths in use. This also shows that when nothing is done to the absorbing material, there is very little absorption, which means the device will operate in the "on" or highly reflective state. To achieve the "off" or low reflective state, some change must occur to the absorption spectrum of the quantum well material. The simple solution is to shift the absorption edge to the larger wavelengths. Figure 2.12 shows an example of the desired effect just mentioned. Now the wavelengths of interest no longer see low absorption, but now see an elevated level of absorption.

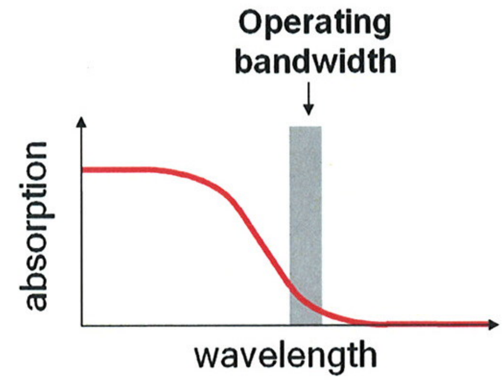

Fig. 2.11. Example absorption curve in relation to range of interest

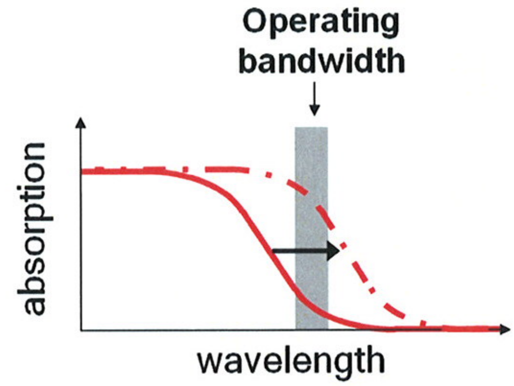

Fig. 2.12. Example of shifting absorption

2.3 Stark Shift

The shifting of the absorption spectrum is accomplished by the application of an electric field to the quantum well material. This effect is called the Stark shift. The minimum energy allowed in the wells is related to the edge of absorption, and the minimum energy can be changed by the applied electric field. The applied field causes band bending in the intrinsic region of the device, as shown in Figure 2.13. The result of this shift is an apparent reduction in the barrier on one side of the quantum well. This reduction lowers the minimum energy allowed above the well potential and allows larger wavelengths to be absorbed. This change in absorption

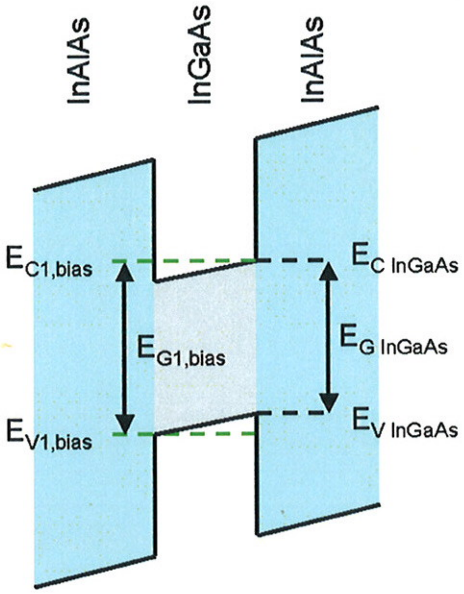

Fig. 2.13. Quantum well under electric field and reduced minimum energy absorbed

gives the appearance of a shift to larger wavelengths or lower frequencies. The ideal case shown in Figure 2.12 is not exactly how the shift occurs. Instead, as the shift increases, the absorption edge gets flattened out. Figure 2.14 has a plot of the actual data from an observed shift.

2.4 Exciton

In Figure 2.14, the absorption edge is characterized by a peak in absorption before the drop-off. This peak is due to a Coulombic force attraction between an electron and hole called an exciton. The exciton can reduce the bandgap of the material by a small amount equal to the energy that holds the electron and hole together

$$E = \frac{\mu_{eff} e^4}{8h^2\epsilon^2} \tag{2.7}$$

[26]. Excitons can exist in bulk semiconductors under certain conditions, but an applied field can easily overcome the exciton binding energy destroy the exciton. In

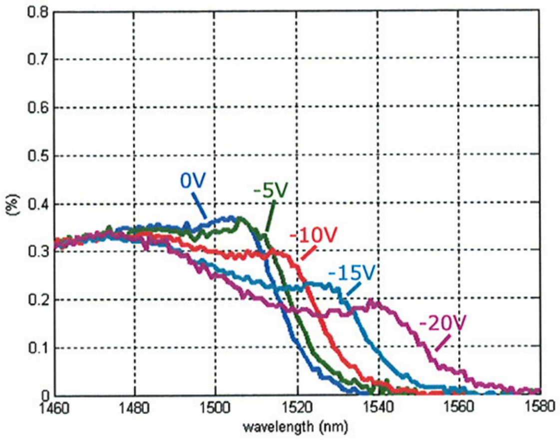

Fig. 2.14. Examples of absorption with exciton peak for different voltages

the absorbing quantum well material of the device, electron-hole pairs are physically confined to the well regions of the absorber. Now, if there is an applied field, the exciton can still exist since the electron and hole are still in close enough proximity to each other. Figure 2.14 still shows a peak when the applied voltage is at -20V. Under extreme fields due to large applied voltages, the electron and hole can escape the confinement of the well and thus removing the effect of the exciton [27]. This has been observed with applied voltages lower than -35V.

To summarize, the modulator functions at a certain wavelength between two states of low and high reflectivity. The high reflectivity state is characterized with little absorption at the wavelength of interest, and the low reflective state is characterized by that same wavelength exposed to higher absorption due to a shift induced by an applied electric field.

3. DEVICE FABRICATION AND DC TESTING

3.1 Wafer Growth, Measurement, and Preparation

Current devices are being fabricated on material grown from a commercial growth vendor. The specific materials required to construct the desired modulator are grown by molecular beam epitaxy on an InP wafer. The wafer growth is shown in Figure 3.1. The device is actually a P-I-N diode operated in reverse bias, where the quantum wells are the intrinsic material. This reverse bias provides the electric field necessary for shifting the absorption edge. Once received, the wafer undergoes spectral analysis, as shown in Figure 3.2. A broadband source is used to provide a large bandwidth (1300-1700nm) of light for testing. The monochromator selects a very small portion (<1nm) of the supplied spectra, and is varied throughout the above range. The light from the monochromator is focused on the bottom side of the wafer, as shown in Figure 3.3 and the transmitted and reflected light is measured at intervals of 1nm. The absorption of the material is determined from the transmission and reflection measurements. This is performed to ensure the grown material has the specific characteristics to ensure

InGaAs	p+ contacting layer	300Å
InAlAs	p-type spacer layer	2500Å
	Quantum wells – 80 periods	
InGaAs	well material	74Å
InAlAs	barrier material	70Å
InAlAs	n-type spacer layer	3000Å
	DBR reflector – 8 periods	
InAlAs	low index material	1219Å
InAlGaAs	high index material	1138Å
InP	substrate	~500um

Fig. 3.1. Wafer growth table

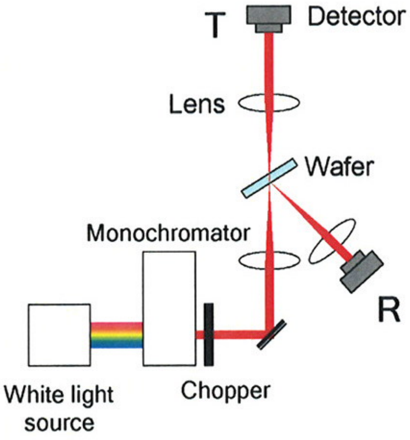

Fig. 3.2. Wafer spectral measurement setup

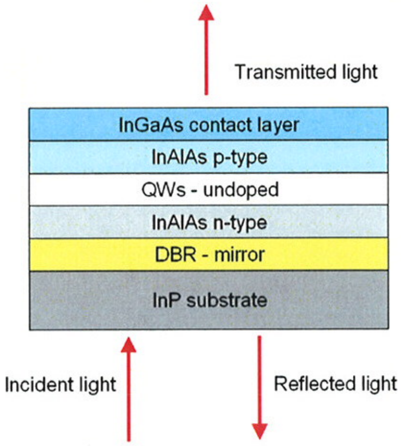

Fig. 3.3. Light interacting with the wafer

device functionality. This includes determining what wavelength the absorption edge resides, at what wavelength the DBR is centered, and other general optical flaws. Once the testing is complete, the wafer is diced into 8x8mm pieces and semiconductor processing is begun. Each wafer piece will contain many devices of varying size, test and alignment patterns, and multiple arrays of different device sizes. Figure 3.4 shows the many structures to be fabricated on the wafer piece. Fabrication is performed at the Purdue Birck Nanotechnology cleanroom facility.

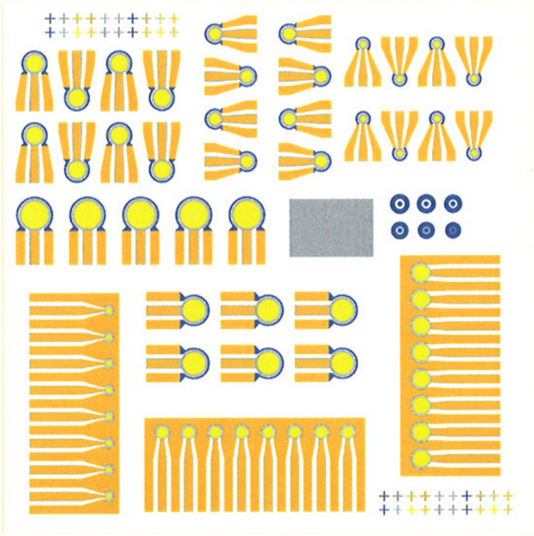

Fig. 3.4. Overview of device processing mask

3.2 P-ohmic Contacts

The first fabrication step in making a single device is to evaporate, using electron beam evaporation, ohmic contacts to the p+ contacting layer on the top of the wafer. The p-ohmic contacting metal consists of 200Å Ti, 200Å Pt, and 2000Å Au in a ring-like pattern show in Figure 3.5. A profile display of the device at the location indicated by the red line of the previous top down display is shown in Figure 3.6. All of the patterning for any fabrication step is performed by spinning a thin layer of photoresist onto the piece, then exposing the desired area of the pattern to ultraviolet (UV) light. A develop step will remove any photoresist exposed to UV light, exposing the material beneath. Now, with exposed material, metals can be evaporated on a desired area or material can be etched away. Any residual metal and/or photoresist can now be removed with solvents.

3.3 Mesa Etch

After the first ohmic step, a mesa etch will be performed to expose the lower n-type material. The mesa will surround the previous p-ohmic metal ring and extend

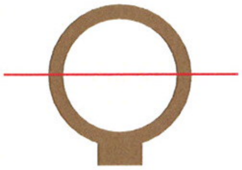

Fig. 3.5. P-ohmic contact step, top down view

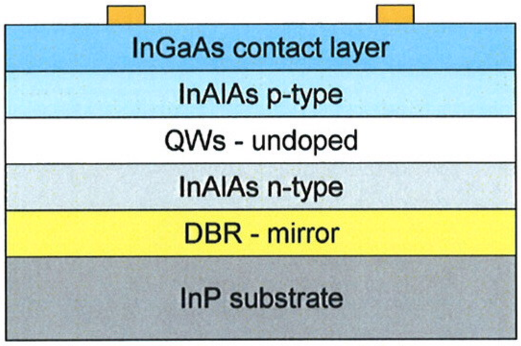

Fig. 3.6. P-ohmic contact step, profile view

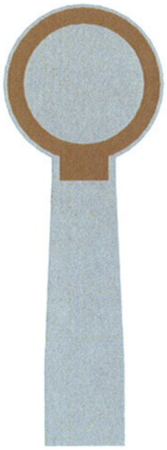

Fig. 3.7. Mesa etch step, top down view

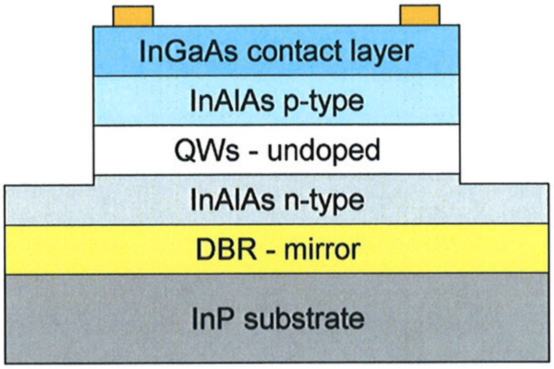

Fig. 3.8. Mesa etch step, profile view

far below the active area (the area in the ring) of the device, as shown in Figure 3.7 and Figure 3.8. This will provide an island or mesa of some n-type material with both the quantum wells and p-type material on top. The etch is performed by patterning photoresist to cover the desired area and etching everywhere else with a wet etch process of H_2O_2:H_3PO_4:H_2O (hydrogen peroxide : phosphoric acid : ultra pure water) 1:1:75. This etch is a timed etch at the rate of ~10Å/sec and is performed in steps with depth checks using a profilometer to assure an etch depth into the n-type semiconductor.

3.4 N-ohmic Contacts and I-V testing

Once the material is exposed, a horseshoe pattern of n-ohmic metals (Ni-100Å/Ge-100Å/Au-200Å/Ge-100Å/Au-200Å/Ni-100Å/Au-1800Å) is deposited using the same e-beam evaporation technique mentioned in the previous ohmic step. Figure 3.9 and Figure 3.10 show the top-down and profile views of this step respectively. After both ohmic metals have been deposited, electrical current-voltage (I-V) measurements

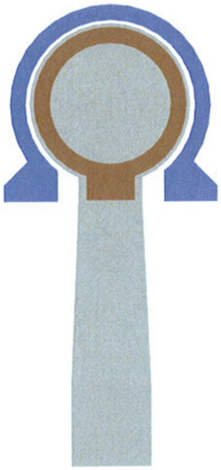

Fig. 3.9. N-ohmic contact step, top down view

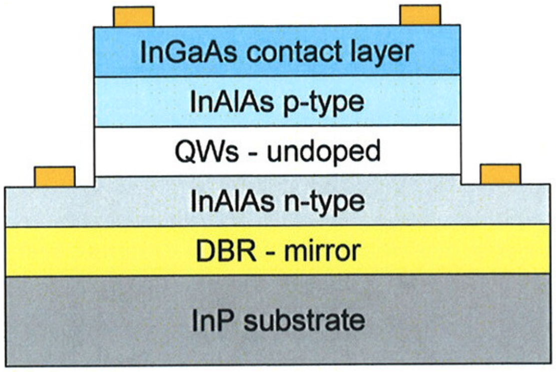

Fig. 3.10. N-ohmic contact step, profile view

are obtained using a semiconductor parameter analyzer to ensure that the material functions like a diode and to ensure the contacts are ohmic. Figures 3.11 and 3.12 show the n-ohmic contact and the p-ohmic IV curves respectively of a previous set of

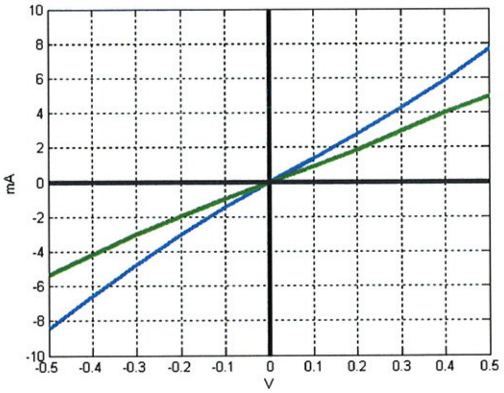

Fig. 3.11. N-ohmic I-V plots

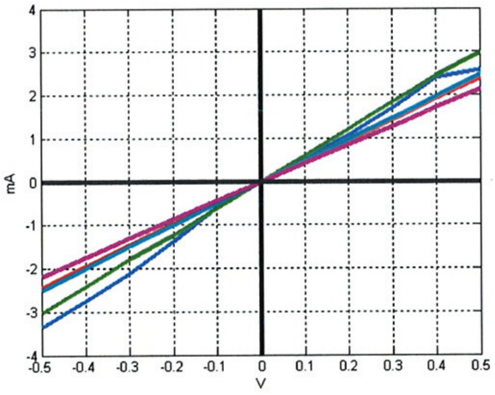

Fig. 3.12. P-ohmic I-V plots

fabricated devices, while Figure 3.13 shows the IV curve of the device. The current indicates diode functionality and Figure 3.14 shows a zoomed in look at the reverse bias current, since this is closer to the desired operating voltage.

3.5 Coplanar Waveguide and Biased Spectral Measurements

When the ohmic steps have been completed, metallic landing pads are evaporated on the edges of the ohmic contacts to provide any easy way to supply a bias at a safe distance to reduce the possibility of damaging the active area, where the light will go through, and to keep the probe tips that will supply the bias from blocking any light through the device. These landing pads are also a 50Ω waveguide for the impedance matching desired in high frequency testing. Figure 3.15 shows the top-down view of this step. There is no change in the profile view of the active area from the previous step. The next step is to measure the transmission and reflection of the device shown in Figure 3.15 (and profile view in Figure 3.10) with a bias. This ensures that a shift in the absorption curve occurs when the voltage is applied. The device is placed in another optical setup, shown in Figure 3.16 used to focus light through the bottom InP substrate of the device while applying a voltage through the waveguide pads. Figure 3.17 shows an example of this. A tunable continuous

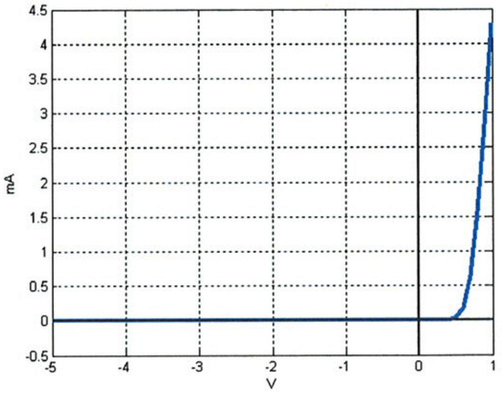

Fig. 3.13. Device I-V curve

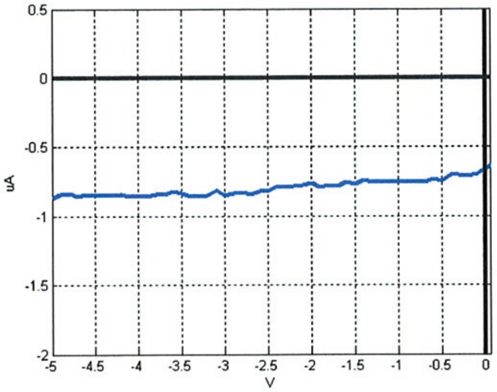

Fig. 3.14. Close view of reverse bias current

Fig. 3.15. Top down view of waveguide step

wavelength (CW) laser is used to provide a narrow spectral source varying from 1460-1580nm in 1nm steps, while detectors again measure reflected and transmitted power. Another detector is used to measure the input power as a reference, and the device absorption is again determined from the reflection and transmission measurements. An infrared (IR) camera is used to position the active area of the device within the beam path. Applying a voltage through probe tips allows the measurements to be performed for varying biases and the change in absorption can be determined for these different voltages. Figure 3.18 shows the device absorption for varying voltages, and Figure 3.19 shows the absorption difference which is calculated by subtracting the absorption at the applied voltage from the absorption at the zero bias voltage (A_V-A_0). With the change in absorption for varying voltages, we can now see where a good operating range would exist. Having a large change in absorption gives an indication of the wavelength region of interest, but is not the only criteria. A large change in absorption could occur at high voltages due to the large shift in the absorption, but looking at Figure 3.18, larger voltages also flatten out the absorption curve to a lower value. If the value is suppressed below a certain value, there will not be enough

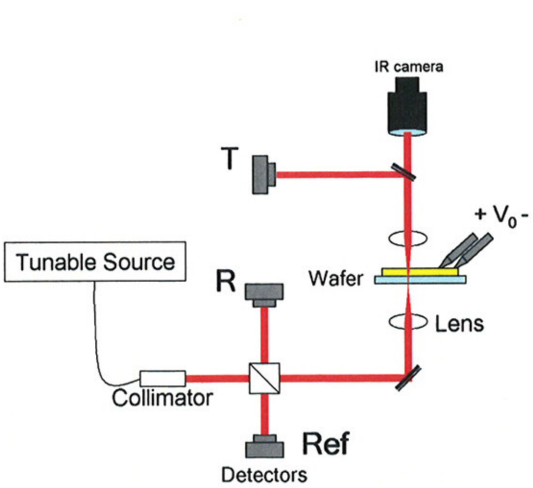

Fig. 3.16. Device spectral measurement setup

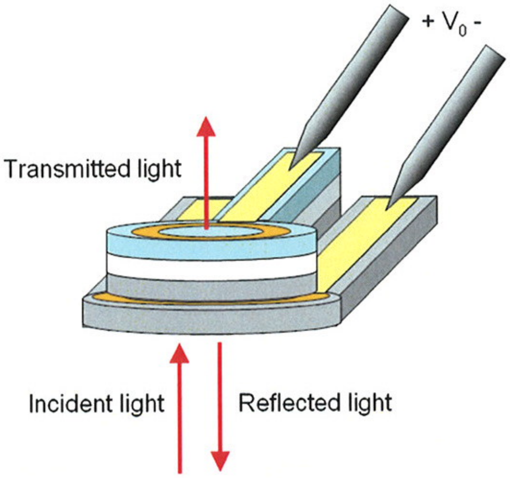

Fig. 3.17. Light interaction and applied bias upon device

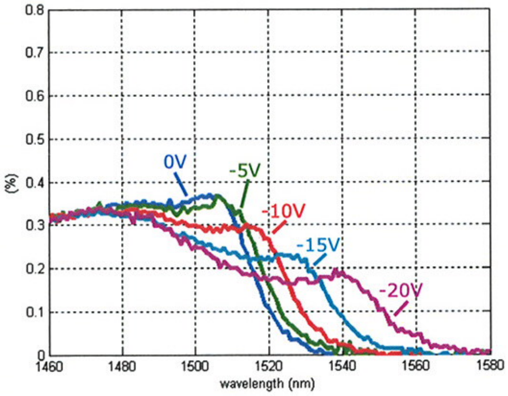

Fig. 3.18. Device absorption for varying applied voltages

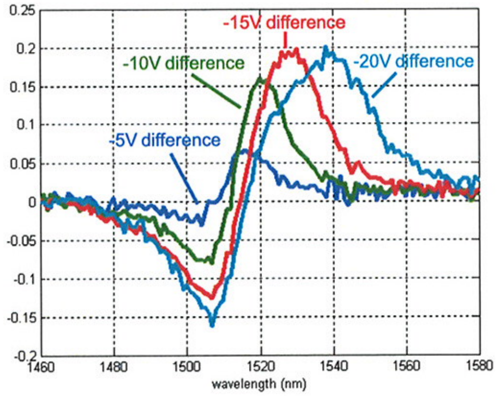

Fig. 3.19. Device absorption difference for varying voltages

absorption to create the effect of reducing the back reflector value to produce the low reflected power reflected in the "off" state. This now becomes an optimization of device performance while maintaining the reflection requirements of the "off" state, and computer simulations assist with this task to determine the best applied voltage and optimum cavity length. The absorption information for applied voltages allows the computer simulation of what the performance of a completed device would look like. Given an applied voltage of -10V, the optimal operating wavelength is ~1520 nm with an "off" state reflected power of <2% and an "on" state reflected power of >31%, a contrast ratio of 15.5 or 11.9dB. The current device under test is without a back mirror and without the cavity optimized to yield a minimum power "off" state with maximum contrast between the states. A simulation of the device with varying cavity length and rear mirror will determine where the optimal performance exists. Once the etch depth has been determined, the next fabrication step is to remove some of the top p+ semiconductor material and depositing a metallic mirror after etching. This etching step provides a variable distance between the front and back reflectors. This, in turn, tunes the cavity to operate at the wavelength where the difference between the "on" and "off" reflected powers is maximum. Photoresist is again patterned only exposing the active area of the devices. The wafer piece has material removed using the previously mentioned etch step in small 240Å intervals (~24s). Between each interval, the device is again measured with and without bias in the device measurement setup. Figure 3.20 shows the profile view of the active area with the material etch. The data for each etch step is then compared to a computer simulation of the device without the back mirror and both with and without bias going through 240Å steps of material removed. The computer simulation of the device at the optimal cavity length is used as a guide during the etch process. Once the plots of the device match that of the computer simulation, the optimal cavity length has been reached. The optimal cavity length should be obtained within 11 etch steps, or 2.64kÅ of material removed. The InAlAs p-layer and InGaAs p^+ contacting layer were designed with a combined thickness such that at least one resonance condition

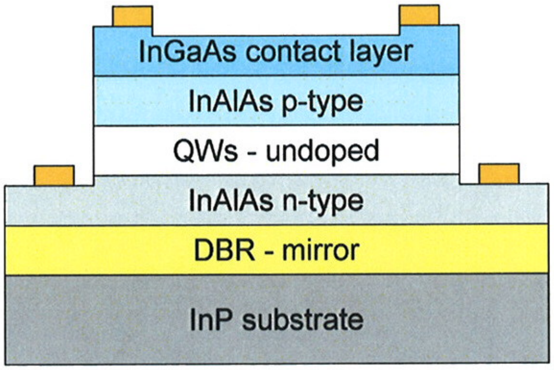

Fig. 3.20. Profile view of tuning etch step

should occur during the tuning etch. Those two layers provide a total optical path length of $\sim 1.82\mu m$ ($>2\pi$ around 1520nm) assuming a material index of 3.2 and 3.65 for InAlAs and InGaAs. A flow chart of the process is shown in Figure 3.21, and

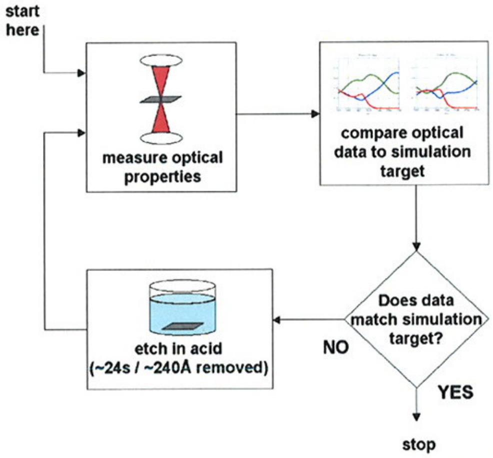

Fig. 3.21. Flow chart of the tuning etch process

the final decision plots are shown in the following figures. Figure 3.22 shows as simulation of what the device should look like with no applied bias at the optimal cavity length, and Figure 3.23 shows the data from the actual device corresponding to the simulation. Not only is the comparison of the simulation to the actual device used, but the plots under a -10V bias are also compared. The -10V simulation and

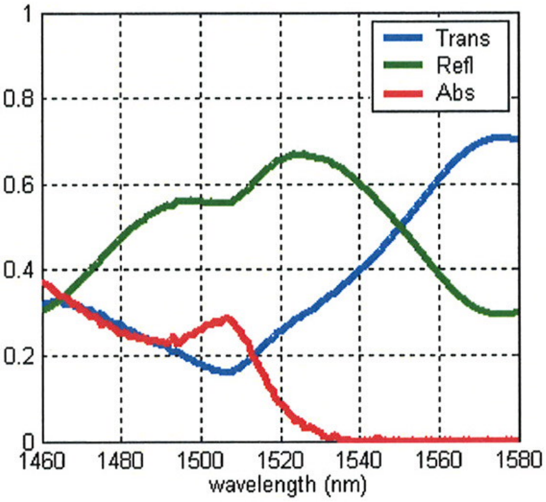

Fig. 3.22. Device simulation after etching, no bias

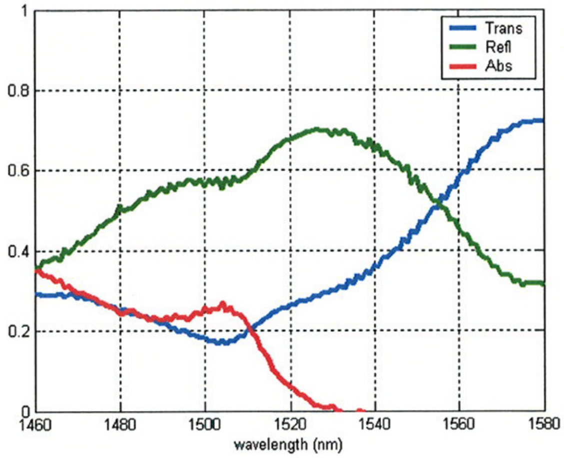

Fig. 3.23. Device measurement after etching, no bias

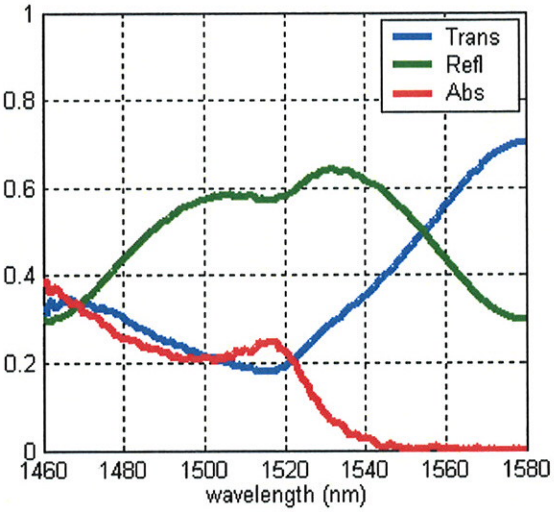

Fig. 3.24. Device simulation after etching, -10V bias

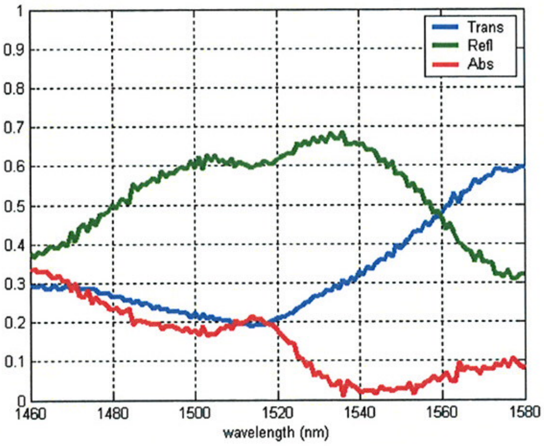

Fig. 3.25. Device measurement after etching, -10V bias

device data plots are shown in Figures 3.24 and 3.25 respectively. There may be a slight amplitude offset between the simulation and data, but that is not the only metric for comparison. The difference between the two peaks of the reflection curve is what changes with longer etch time and it is primarily used for the comparison. The measurements from the steps before reaching the optimal cavity length are also compared to a simulation to ensure the etch process is progressing normally.

3.6 Rear Mirror

When the etch has concluded, the device has a rear mirror of 100Å Ti and 2000Å Au deposited via electron beam evaporation, where the thin Ti layer is used to promote adhesion to the semiconductor. Figures 3.26 and 3.27 again show the top-down and profile views of this last step. Finally, the completed device undergoes another set of measurements in the device testing setup to determine its performance. In this final measurement, only the reflected power can be measured since there is

Fig. 3.26. Mirror step, top-down view

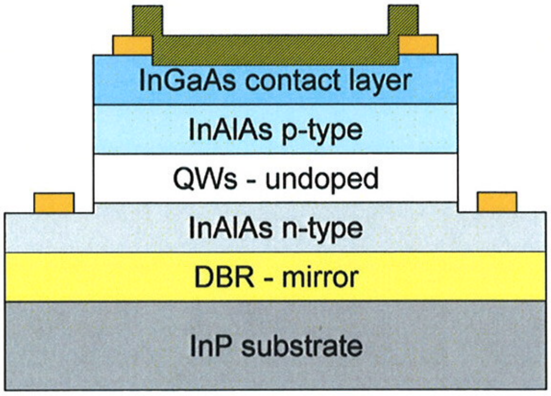

Fig. 3.27. Mirror step, profile view

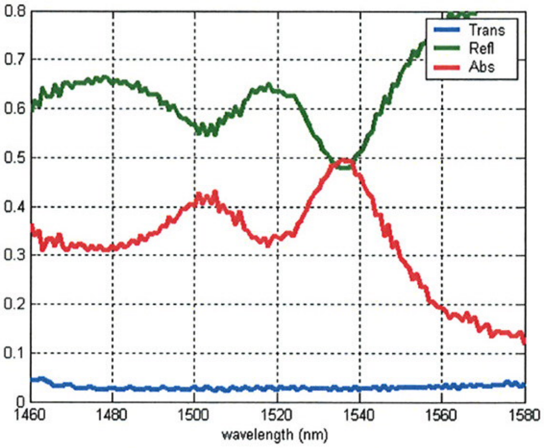

Fig. 3.28. Device measurement after back mirror, no bias

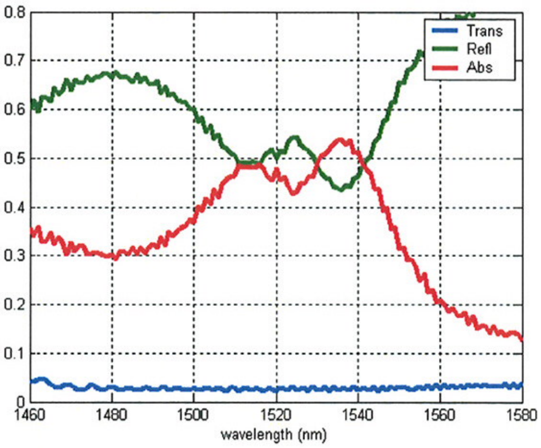

Fig. 3.29. Device measurement after back mirror, -10V bias

a mirror covering the top of the device allowing no light to be transmitted. Figure 3.28 and Figure 3.29 show the reflection and absorption in the device under zero bias and -10V applied respectively. Since we desire low reflectivity in the applied voltage or "off" state, the reflection difference is taken by subtracting the reflection at the applied voltage from the reflection at zero bias (R_V-R_0). The reflection difference plot is shown in Figure 3.30. The results from this piece are not what were expected. The plot in Figure 3.29, where the device is under bias, should have a minimum reflection of 30% in the 1520nm region. The 30% minimum would indicate that the device would operate with a close to zero reflected power in the "off" state when an anti-reflection coating is applied to the bottom of the substrate to cancel the air-InP reflection. The devices (with the back mirror) should have spectral characteristics similar to the computer simulations shown without bias in Figure 3.31 and with -10V applied in Figure 3.32. Since the 30% reflection goal is not apparent in the actual device, it will not have the low power "off" state desired.

The cause for the discrepancy comes from the mirror that was deposited in the previous step. In semiconductor processing, when one wants to place a conducting

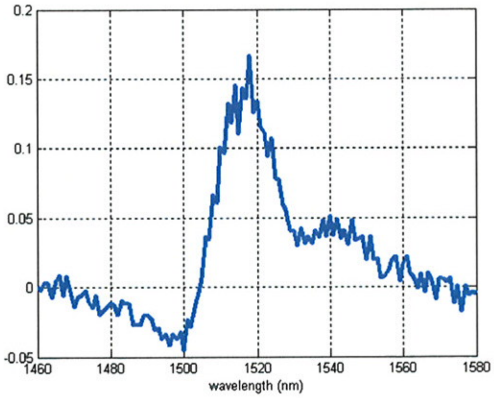

Fig. 3.30. Reflection difference of the device after back mirror

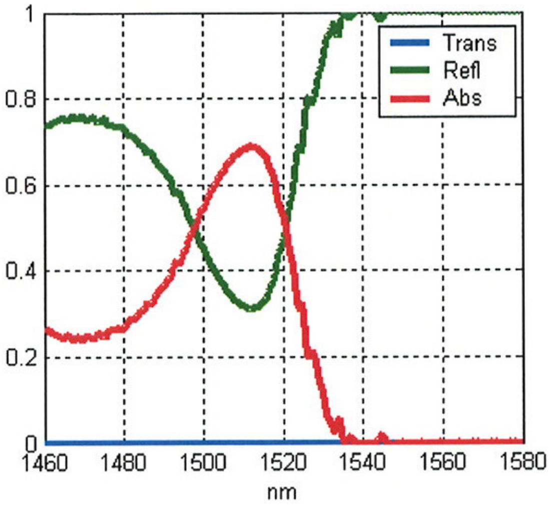

Fig. 3.31. Simulated desired response of device with mirror, no bias

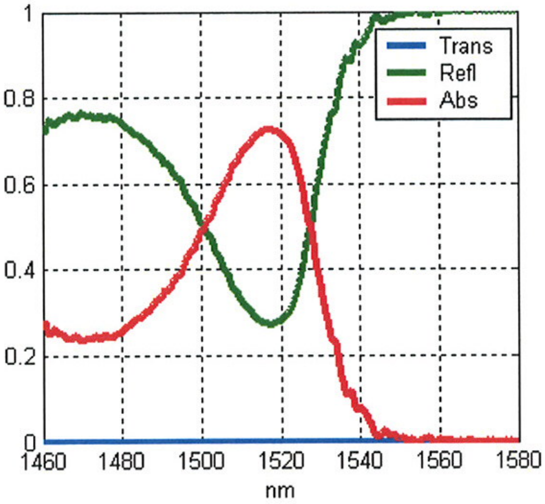

Fig. 3.32. Simulated desired response of device with mirror, -10V bias

strip of metal a combination of a thin layer of titanium and a thick layer of gold is used. The thin (~100Å) layer of titanium is commonly used as an adhesion layer, promoting good physical contact to a semiconductor surface. This recipe works does not work well as an optical mirror. Optical properties of thin deposited Ti films can largely vary depending on the wavelength, thickness of the film, and the amount of oxidation of the film (which can be a function of deposition rates) [28, 29]. Using a deposition rate ~1Å/s could result in an oxidized thin film of titanium with some absorbing properties and an unknown phase change at the semiconductor/titanium interface. This was proven by evaporating the typical Ti/Au and just a Au layer onto separate pieces of an InP substrate. Figure 3.33 shows the reflection, transmission, and absorption of the Ti/Au layer on the InP substrate. Note that there is ~30% absorption in this case. Figure 3.34 shows the same spectral data for just a Au layer on InP. Absorption in this case is substantially smaller, ~5% and is reasonable for usage as a mirror. The phase change due to the addition of either mirrors can be

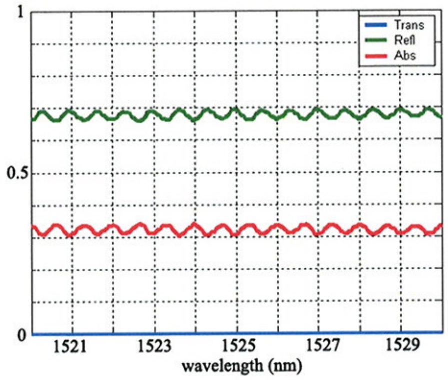

Fig. 3.33. Spectral characteristics of titanium/gold mirror on InP

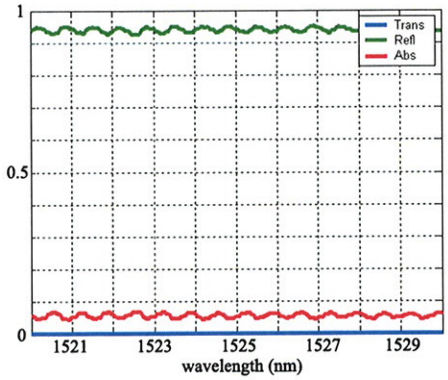

Fig. 3.34. Spectral characteristics of gold mirror on InP

estimated by observing the spectral shift in the peaks and nulls of the reflection data. The estimated phase change for the Au on InP and Ti/Au on InP was $\pi/4$ and π respectively. Lastly, a third test piece had a Au only test mirror evaporated on it. Instead of using a piece of InP only, this last piece had approximately 1500Å of InAlAs on the InP substrate. For the actual devices, the material for which the gold mirror will be evaporated upon is InAlAs. This was a check to see if there were any adhesion problems and to see if the optical performance was similar to the Au on InP case. No adhesion issues were noted and optical performance was similar, as seen in figure 3.35. Instead of simulating the devices with the appropriate absorption and phase change associated with the gold mirror, a more experimental approach was used. Within the entire wafer piece is a set of six 200μm devices, as shown in figure 3.36. In order to determine the correct etch depth to create resonance at the largest absorption change, each of the devices were etched at progressively different depths, from zero to ~1200Å of material removed in ~240Å steps. After all the etches were performed, the rear gold mirror was evaporated onto the device. Spectral measurements of the reflection and transmission were made for varying bias conditions (0, -5, -10, and -15V) for each of the six devices. The device with ~480Å of material removed yielded the best performance and best matched simulations under a -10V bias. Figures 3.37 and 3.38 show the device measurements and simulations respectively.

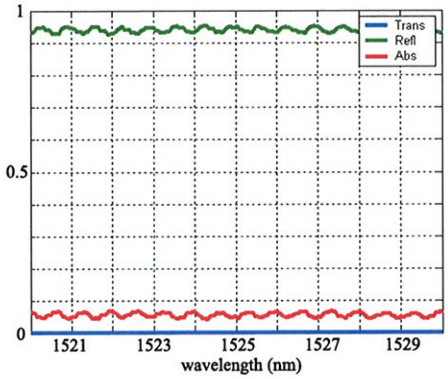

Fig. 3.35. Spectral characteristics of gold mirror on InAlAs

Fig. 3.36. Selected devices for varying etch test.

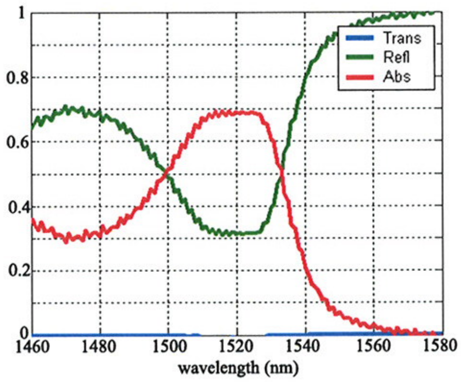

Fig. 3.37. Data from device with back mirror under -10V bias

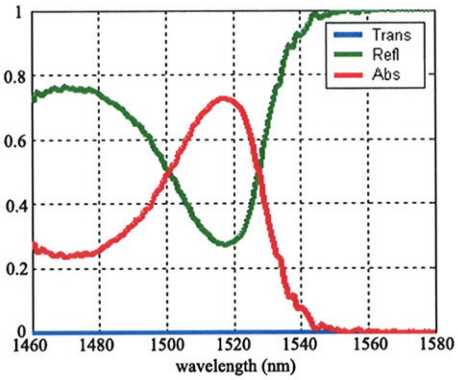

Fig. 3.38. Simulation of device with mirror under -10V bias

3.7 Anti-Reflective Coating

Now that the proper etch depth has been determined for device resonance, the next step is to deposit an anti-reflective (AR) coating to the bottom of the InP substrate. This would reduce or eliminate the ∼30% reflection seen when considering the air/substrate interface. Since a low reflected power "off" state is desired, this would greatly improve the device performance from the case without the AR coating. A common metric used for modulators is called contrast ratio, which is calculated by dividing the reflected power in the "on" state by the power in the "off" state. Having close to zero power in the denominator due to low "off" state power would yield a very high contrast ratio. Zero reflection would be achieved if the index of refraction of InP was the same as that of air. The same statement could be made if the characteristic impedances were equal since it is related to the index by

$$\eta = \frac{\eta_0}{n} \tag{3.1}$$

where η is the characteristic impedance of the material, η_0 is the characteristic impedance of free space, and n is the index of the material. In order to minimize reflection the characteristic impedance of the combination of the AR coating plus the InP substrate must be close to that of air. The impedance of the combination can be expressed as

$$\eta_{AR+InP} = \eta_{AR}\left[\frac{\eta_{_{InP}} coskl + j\eta_{_{AR}} sinkl}{\eta_{_{AR}} coskl + j\eta_{_{InP}} sinkl}\right] \tag{3.2}$$

where k and l are the propagation constant and the thickness of the AR layer respectively [30]. The propagation constant is defined as k=$2\pi/\lambda$, where λ is the wavelength within the AR material. Setting equation (3.2) equal to the characteristic impedance of air (η_0) and setting the thickness of the AR layer l=$\lambda/4$ will allow us to start solving for the impedance of the AR coating. The quarter wavelength AR thickness is not the only solution. Any of the values $\lambda/4 + n\lambda/2$ will obtain the same results when n is equal to any positive integer. For simplicity, the thinnest amount of material needed is chosen. Now,

$$kl = \frac{\pi\,(1+2n)}{2} \tag{3.3}$$

then $cos(kl) = 0$ and $sin(kl) = 1$, leaving

$$\eta_0 = \eta_{AR}\left[\frac{\eta_{AR}}{\eta_{_{InP}}}\right] \tag{3.4}$$

Using the relationship η=$\sqrt(\mu/\epsilon)$ and the equation

$$n_{_{AR}} = \sqrt{\epsilon_{_{r,AR}}} \tag{3.5}$$

and by rearranging terms, equation (3.4) becomes

$$n_{AR} = \sqrt{n_{InP}} \tag{3.6}$$

This last equation simply states that the index of refraction of the AR coating should be the square root of the index for the InP substrate. Using the index of InP at 1520nm, n_{InP}=3.17 and n_{AR}=1.78. This index is close to that of aluminum oxide (alumina) which is ~ 1.746 at 1550nm for bulk material (and can also vary for thin films) [31–33]. A calculation the air-alumina-InP structure yields a reflected power of $< 0.2\%$ at 1520nm when using the index of 1.746 for the alumina layer with a quarter wavelength thickness.

The next step is to deposit alumina on the bottom side of the substrate. This will be done via electron beam evaporation. Small alumina pellets are placed within a tungsten carbide crucible and are heated by a stream of high energy electrons and evaporated under high vacuum. In order to achieve optimal results, a few trial evaporations were performed by evaporating alumina onto the polished surface of a single-side polished (SSP) InP wafer. The reason for using the SSP wafer is to avoid having multiple reflections between the two polished surfaces of the substrate. The rough back surface should scatter the incident light, providing little back reflection. The first trial case was performed by evaporating ~2176Å of alumina, where the target was 2135Å. Now the sample piece has its reflectivity measured over a broad spectrum. The device measurement setup is used to perform this, and the result is shown in figure 3.39. The minimum of the reflectivity should be in the neighborhood of 1520-1530nm, but it actually around 1300nm. This means that either the thickness or index of the material is incorrectly represented. The thickness of the AR material was measured using a profilometer, a device that measures small thicknesses by dragging a probe tip across the surface of the material and observes height changes. The profilometer indicated that the thickness of the material was ~1600Å. This is substantially different than the indicated thickness during deposition. In order to better understand the characteristics of the material, a simulation was performed to match the spectral reflectivity. Figure 3.40 shows the data compared to the simulation. The simulation

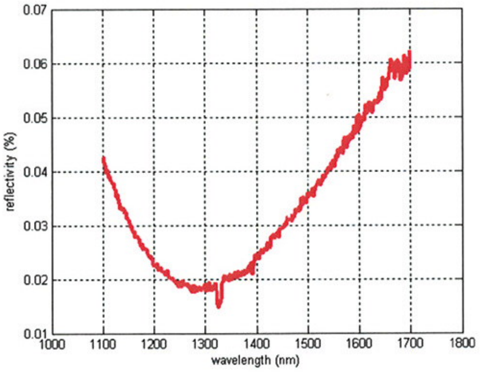

Fig. 3.39. Reflectivity of first attempt of AR on InP.

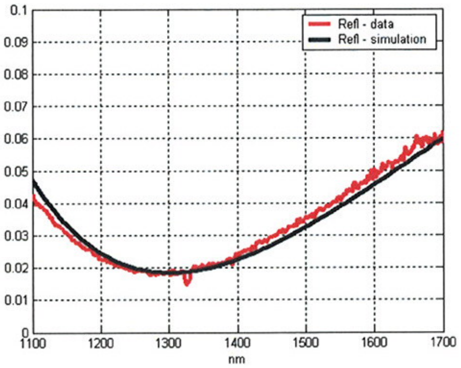

Fig. 3.40. Reflectivity of first attempt of AR on InP along with simulated data.

uses the thickness determined from the profilometer, and has an adjusted index of refraction of 2.05. A second evaporation of the AR coating was attempted using the information from the first deposition. A correction factor was used to match the thickness indicated on the evaporation system and the actual measured thickness. The second trial resulted in an AR layer with a thickness of 1977Å and the spectral reflectivity is shown in figure 3.41. Again, the minimum reflectivity is not centered at the desired wavelength. The profilometer indicated thickness was 1971Å, which is quite close to the indicated amount during the evaporation. A simulation of the AR layer was performed, same as the first attempt, do determine the index of the material. Figure 3.42 shows the data along with the simulation approximation. The index used

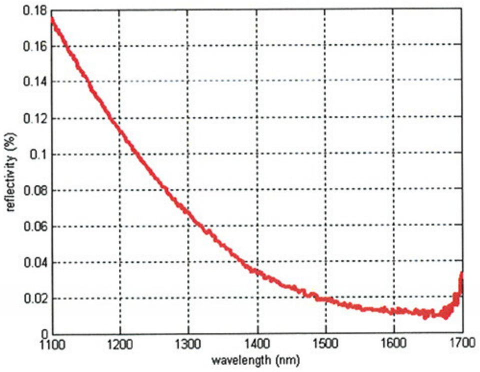

Fig. 3.41. Reflectivity of second attempt of AR on InP.

in this simulation was 1.95. The variance in the AR index could be explained by

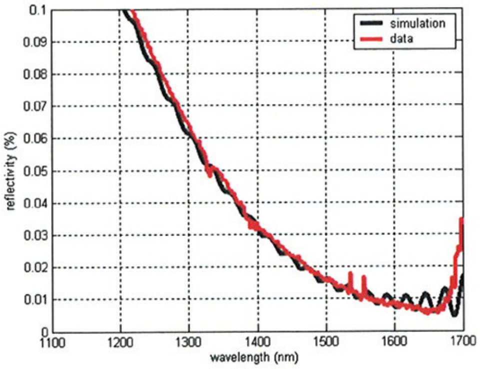

Fig. 3.42. Reflectivity of second attempt of AR in InP along with simulated data.

differences during the evaporation process. All of the alumina pellets in the crucible did not melt during evaporation. Material melting was very local and evaporation rates varied widely depending on whether the electron beam was hitting material or gaps between pellets. Such variation could cause the range of index changes.

With the two attempts yielding reflectivity minima below and above the desired wavelength, a target thickness (which is an average of the two trials) for the AR layer for all the devices was chosen to be 1850Å. The actual deposited material was ~1860Å, and the results are seen on figures 3.43 through 3.46. These figures show the

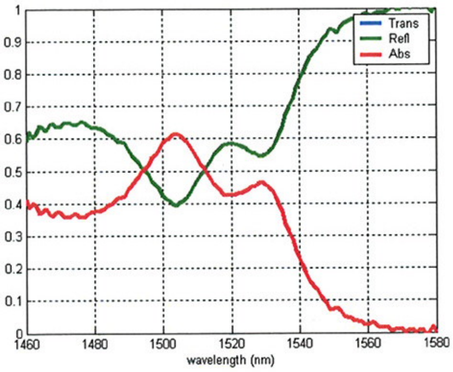

Fig. 3.43. Spectral data from device with back mirror and AR coating with zero bias

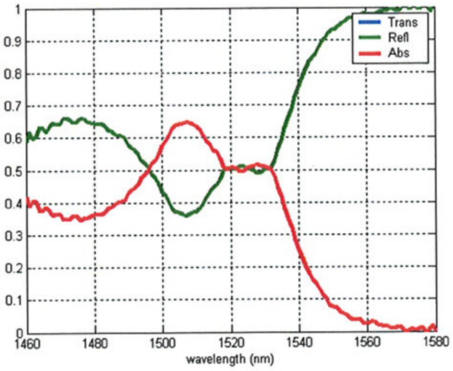

Fig. 3.44. Spectral data from device with back mirror and AR coating with -5V bias

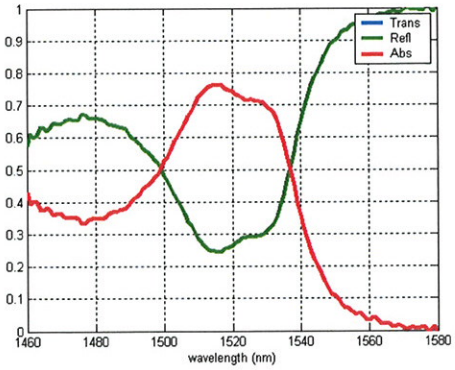

Fig. 3.45. Spectral data from device with back mirror and AR coating with -10V bias

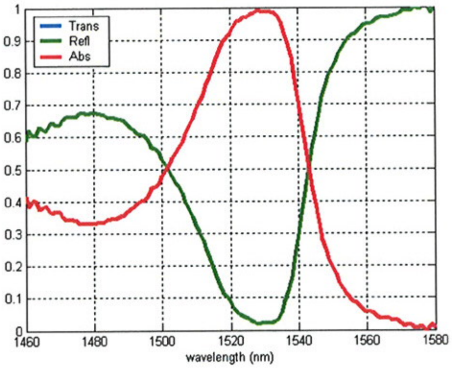

Fig. 3.46. Spectral data from device with back mirror and AR coating with -15V bias

reflection and absorption characteristics for a single device over a certain spectrum for varying biases (zero to -15V in 5V steps).

The reflectivity progression for increasing reverse bias can been seen, and the most important fact to note (figure 3.46) is the close to zero reflectivity in the 1530nm region when the device is under -15V bias. This fact allows the device to switch between a ~60% reflector and a near 2% reflector within a region centererd near 1530nm. Figure 3.47 concentrates on the varying reflectance as the bias is changed.

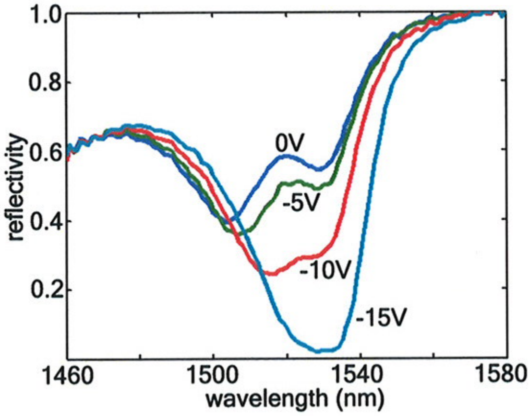

Fig. 3.47. Device reflectivity as bias is changed.

3.8 DC Spectral Extinction Ratio

A common metric for modulator performance is extinction ratio, which is given by

$$r_e = \frac{P_{ON}}{P_{OFF}} \tag{3.7}$$

where $P_{ON/OFF}$ is the optical power from the modulator in the "on" or "off" state. Since this device is a reflection based modulator, the reflected optical power will be observed. The extinction ratio of the device was calculated by observing the reflectivity of the device in one of the DC biased states figures 3.44-3.46, and dividing it by the reflectivity curve in figure 3.43. The extinction for the -15V bias case is shown in figure 3.48, and it shows that the ratio is greater than 20 (13dB) for a spectral bandwidth of roughly 6nm. It is also useful to observe the extinction from -5V bias to -15V bias. Since the goal is to operate this device at RF, a large peak-to-peak voltage drive might be difficult. Reducing the drive from 15V$_{p-p}$ to 10V$_{p-p}$ could ease any driving issues. The extinction for the -5V to -15V case is shown in

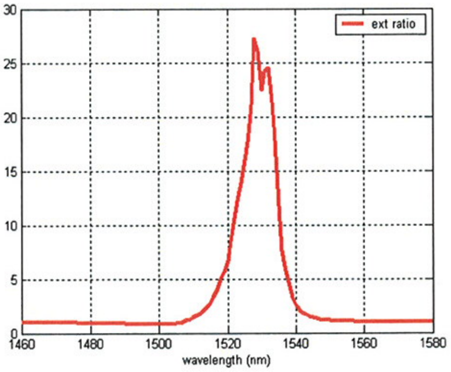

Fig. 3.48. Extinction ratio of device between zero bias and -15V bias.

figure 3.49. Both curves are quite similar and show little performance decrease. This should provide more flexibility for experimentation.

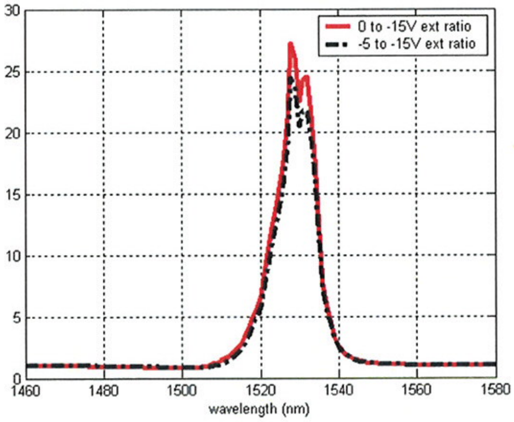

Fig. 3.49. Comparison of extinction ratios between 0V to -15V and -5V to -15V.

4. RF DEVICE PERFORMANCE

In the previous chapter, DC spectral modulation was demonstrated. High speed modulation and testing procedures will be the focus of this chapter. The test setup for observing RF modulation of the devices is shown in figure 4.1. A continuous wave (CW) fiber laser is used as the source, which is input into a circulator. The wavelength of the CW laser is chosen within the band showing high extinction from the previous chapter. The CW light exits the fiber and is directed onto the active area of the device by means of two aspheric lenses. The lenses are arranged such that the light exiting the fiber is imaged onto the device, and any reflected light from the device is coupled back into the fiber. Returned light is sent to an erbium doped fiber amplifier (EDFA), then to a photodetector for optical-to-electrical conversion. The electrical output of the detector is monitored on a high speed oscilloscope. If the modulator is driven with time varying signal lower than that cutoff frequency, the received signal on the scope should also be time varying and should take on the same

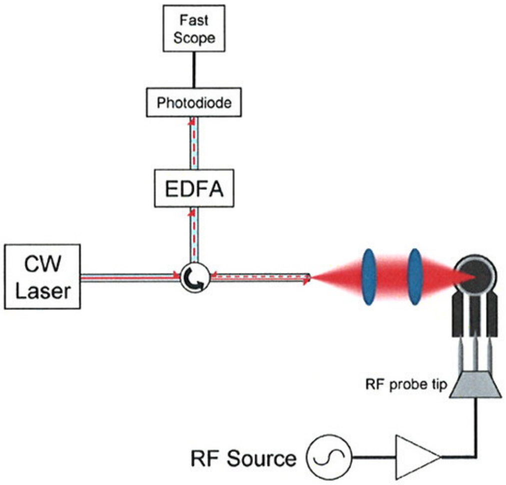

Fig. 4.1. Setup for testing high speed performance of the device.

appearance of the drive signal. The devices are driven by a sine wave generated by a RF signal generator. That signal is amplified and is applied to the device through an RF probe. The RF drive frequency is swept from 10MHz to 10GHZ or until the signal is too small, and the output on the scope is captured by computer. The next few plots in figure 4.2 show the progression of the received signal as the frequency is swept from 100MHz to 5GHz at +18dBm for a 250μm modulator while illuminating the device with 100μW of optical power at 1534nm. The device was also biased at -9V so that the AC drive signal would toggle between the "on" and "off" states of the device. These plots show the amplitude reduction with increased drive frequency. Figure 4.3 shows the normalized AC magnitude as a function of frequency for the same 250μm modulator.

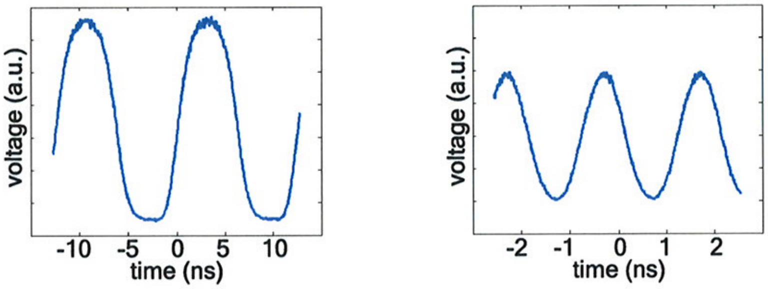

(a) 100MHZ (b) 500MHz

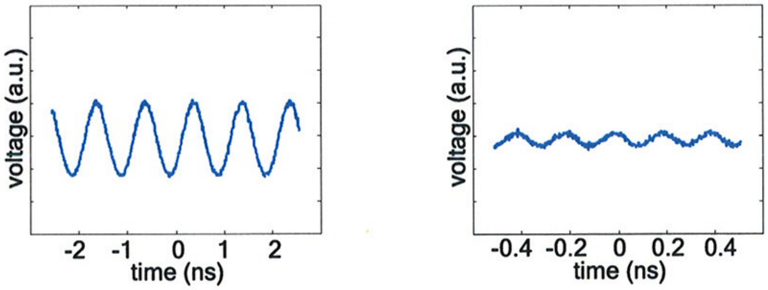

(c) 1GHz (d) 5GHz

Fig. 4.2. 250 μm device under AC testing while varying drive frequency

This method of testing a device while varying RF drive frequency was performed for multiple device sizes. The device sizes along with cutoff frequencies are shown

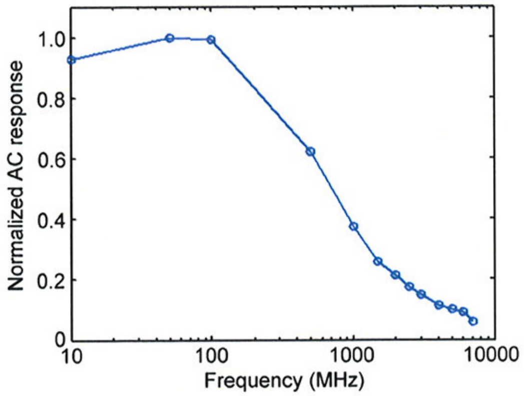

Fig. 4.3. AC response of 250μm device as a function of frequency.

in table 4.1. These results were obtained with the device driven with +18dBm RF power and under laser illumination at 1534nm with 100μW optical power. The cutoff frequency is defined as the frequency when the normalized AC magnitude response is equal to 0.5. The estimated RC cutoff frequency (1/RC), which is calculated by estimating the device capacitance (a function of device area) and assuming a 50 Ω resistance, is also included for comparison. The device nomenclature starts with the type of device, diameter of the active area of the device (the circular portion which can modulate light), and could have the specific device within the group appended to the end. The types of devices could either be within an array "A" or within a group of single devices "D." For example, device A150B would be the second device within

Table 4.1
AC testing of various devices

Device	**Device Area**	**AC Cutoff**	**Est. Cutoff**
D100G	47,201μm^2	1.959GHz	5.2GHz
D150G	64,356μm^2	1.164GHz	3.8GHz
A100F	71,073μm^2	1.158GHz	3.5GHz
A150B	83,536μm^2	922MHz	2.9GHz
D250C	103,686μm^2	703MHz	2.4GHz

an array of 150μm devices. The device capacitance is not just the active area, but also includes the area under the center conductor. This area is equal to the the area of the mesa etch step explained in chapter 3 and an example is shown in figure 3.7. The capacitance can be reduced to roughly the active area, but fabrication complexity would increase dramatically. A plot with the cutoff frequencies versus device area is shown in figure 4.4 along with a curve fitting the data points. The cutoff frequencies are proportional to the inverse of the device area ($f_{cutoff} = K/A_{dev}$), where K is a constant determined by minimizing the mean squared error. The curve is extended to smaller device areas showing the possible operating frequencies for devices with reduced capacitance or smaller device areas.

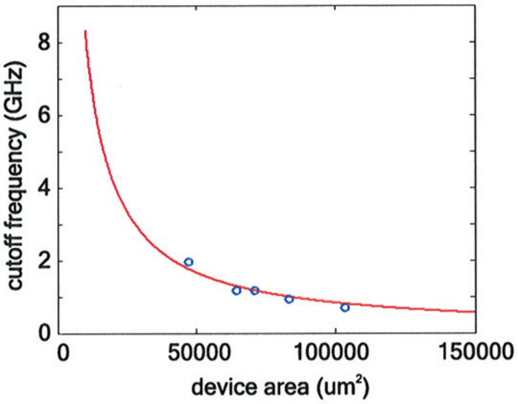

Fig. 4.4. Plot of cutoff frequencies for devices along with curve fitting the data points.

5. DST PULSE SHAPING WITH DEVICE ARRAY

5.1 DST pulse shaping with modified Arrayed Waveguide Grating

The high speed functionality shown in the previous chapter will lead way to the rapid reconfiguration of the spatial pattern used within the DST pulse shaper. First, basic DST pulse shaping using integrated components must be explained. This form of pulse shaping starts with the modified AWG. Typically, AWGs are commonly used as wavelength multiplexing/demultiplexing devices, and an example AWG is shown in figure 5.1 [34]. Light enters one of the many input guides, and reaches the first slab waveguide where the input light illuminates the device waveguide array. The illumination is not uniform since the light exiting the input guide and traveling through the slab waveguide does not have a uniform spatial profile. The light within each of the device waveguides experiences a unique delay due to the fact that all of the waveguides have different lengths. At the end of the waveguides, light exits each guide and travels through another slab waveguide. If the light inserted into the AWG

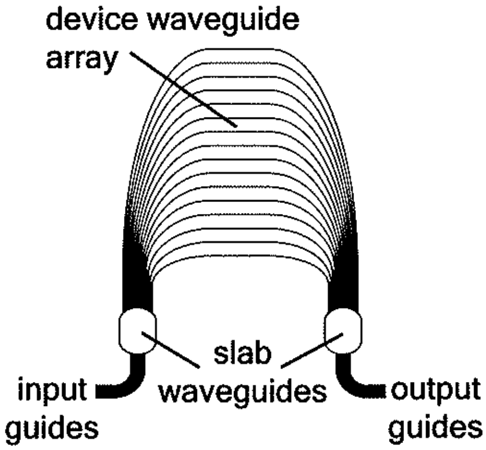

Fig. 5.1. Typical AWG

is CW or always on, constructive/destructive interference will occur at the back of the second slab waveguide with a wavelength dependence. Different wavelength outputs from the AWG can be chosen by selecting different output guides. This functionality can also be observed with pulsed inputs, but the pulse length must be longer than the delay between device waveguides to ensure proper interference. This method of operation is useful, but not conducive for DST pulse shaping. Consider the case of a pulsed input with a pulse duration shorter then the guide-to-guide delay of the waveguide array [35]. Light still enters through the input guides and illuminates the array, but each pulse reaches the second slab waveguide at different times with enough separation between pulses in order to distinguish them from each other. The pulse exiting any of the waveguides then travels through the second slab waveguide and illuminates the output guides without interference from any of the pulses before or after it. Any of the output guides can be chosen to observe the output of the AWG. The output signal of the AWG is a number of pulses (given by the number of guides in the array) in time separated by the guide-to-guide delay. For example, if there is a 1ps pulse input into an AWG with 16 guides with a 5ns delay between guides, the output would be a pulse train of sixteen 1ps pulses separated by 5ns. Figure 5.2 shows an illustration of an AWG used to generate a pulse train, and shows a snapshot of the various short pulse locations within the array (represented by the circles) due to varying waveguide length. Again the intensity of the individual pulses within the output pulse train will not have uniform intensity due to the previously mentioned non-uniform illumination within the slab waveguides, but it can be adjusted if loss is designed into the waveguides to provide a flat profile [36]. If the typical AWG just mentioned were to be modified by being cut in half and had a mirror placed right at the edge of the waveguides, it would still serve the same function by generating a pulse train. The mirror allows a double pass through the waveguides, which provides the same delay as a single pass through an unmodified device. An example of this is shown in figure 5.3. Instead of observing the output through the output guides, the output is observed by selecting another input guide in the modified device. This

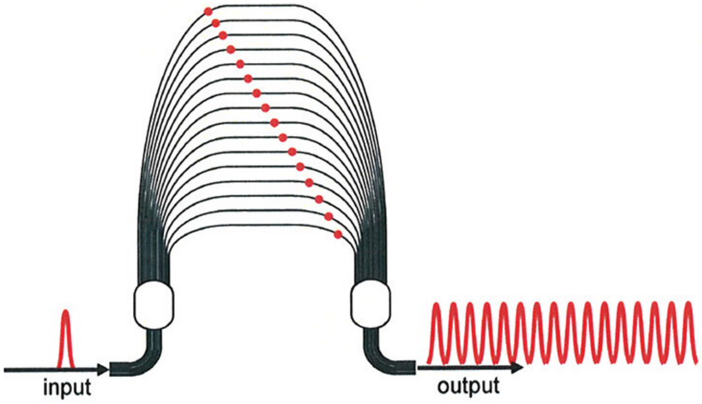

Fig. 5.2. An output pulse train generated by an AWG.

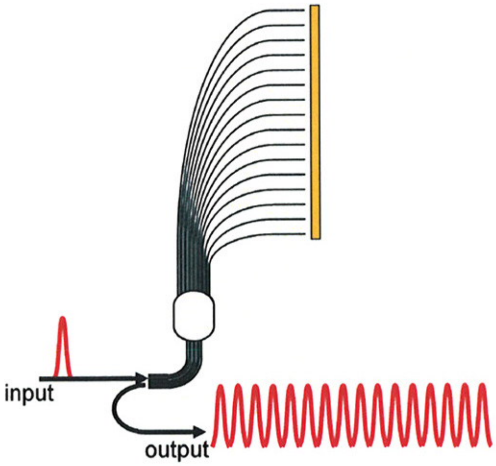

Fig. 5.3. An output pulse train generated by double passing through a modified AWG.

simple form of pulse shaping, by transforming a single short pulse into a pulse train, can be made more intricate and useful if the mirror were to be replaced by a spatial mask which has varying reflectivity as a function of position. Each pulse within the waveguide array of the AWG would have their intensities modified by the spatial pattern and the output pulse train would be a direct time representation of the spatial mask. Figure 5.4 shows an example of integrated DST pulse shaping with a fixed spatial profile. Liquid crystal modulators and micromirrors allow pulse shaper

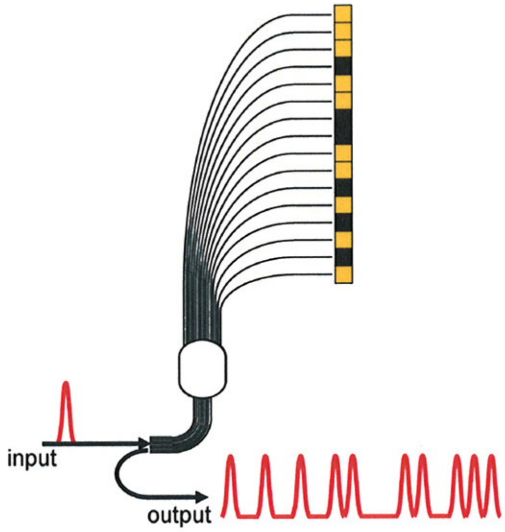

Fig. 5.4. An output pulse train generated by an AWG.

reconfiguration by providing a time varying spatial pattern [12], but update rates are limited from milliseconds down to microseconds depending on the technology used [13–15]. There have been some attempts to increase the pulse shaping update rates using 2-D SLMs, acousto-optical devices, and semiconductor waveguide optical phased arrays with reconfiguration times down to 30ns [16–18]. However, one of the arrays within the wafer piece can be used as a varying spatial profile with update rates near the cutoff frequency of the array device size used.

5.2 Static DST pulse shaping with array of modulators

The above mentioned integrated DST shaping can best be performed using one of the 8x1 arrays of modulators on the fabricated wafer piece. However, using one of those arrays as a spatial profile would require matching the waveguides at the cut end of the AWG with the devices in the array. The AWG used has 16 waveguides with a guide-to-guide spacing of 150μm, and the device array has a device spacing of 250μm. The spacing difference can be resolved by use of a telescope (shown in figure

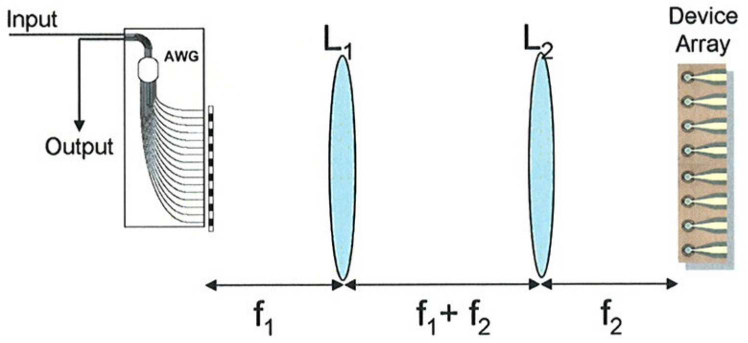

Fig. 5.5. AWG with telescope to match used guides with array of devices.

5.5 by the two lenses), which will properly register the used waveguides to modulators. Figure 5.6 shows a setup that will allow reconfigurable DST pulse shaping with the device array under DC drive. This setup will demonstrate a change in output pulse trains before driving the devices with a high speed signal. The source used within this setup is an actively mode locked fiber laser that produces ∼5ps pulses at a repetition rate of 10GHz. The center wavelength of the source is tunable, and is selected at 1532nm to match the spectral modulation capabilities of the modulator as shown in chapter 3. The output of the laser is connected to a pulse compressor which reduces the pulse duration to ∼400fs. The AWG used has a double pass delay between guides

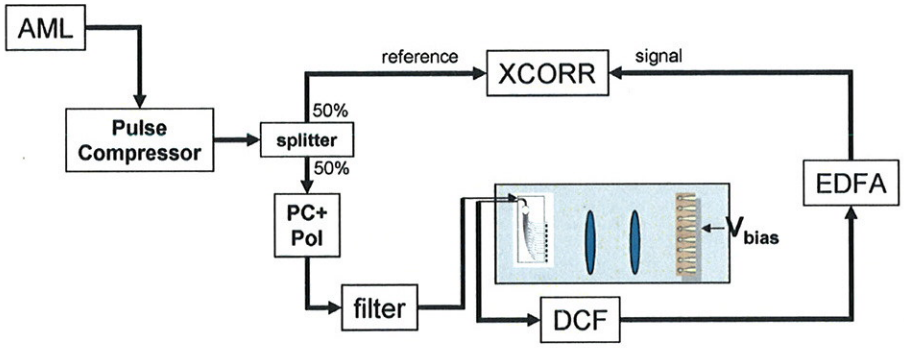

Fig. 5.6. Setup for testing DST pulse shaping at DC rates. Components: actively mode-locked laser (AML), dispersion compensating fiber (DCF), erbium doped fiber amplifier (EDFA), polarization controller (PC), polarizer (Pol), cross correlation (XCORR).

of 1.6ps, and the pulse from the output of the pulse compressor meets the conditions for DST shaping using the AWG. However, the optical bandwidth of the modulators is limited and cannot modulate light outside of its bandwidth which is shown in figure 3.48. A filter must be used to limit the range of wavelengths incident upon the modulator. A 5nm filter was chosen to easily fit within the usable spectrum of the modulator. The pulse duration after the filter is ~1.2ps, which is close the delay between guides. In order to avoid pulse overlap, every other guide will be blocked on the AWG. This yields a round trip delay between used guides of 3.2ps. A tilted mask closely positioned to the output face of the AWG will block half of the guides resulting in only 8 total used guides. Now, the 300μm spacing between used guides must be matched with the 250μm spacing of the devices. A 60mm and 50mm focal length set of lenses will be used as L_1 and L_2 in figure 5.5.

Half of the compressed pulse is sent to the AWG and devices, while the other half is sent to a cross correlation setup as a reference pulse. Cross correlation is the method used for pulse measurement since conventional optical to electrical conversion through the usage photodiodes is too slow to capture the details of the pulse trains generated in these experiments. Cross correlation spatially combines two signals within a second harmonic generation (SHG) crystal, and generates an optical signal at twice the frequency when the intensities of the two signals overlap in time [37]. Obtaining the actual profile of the output pulse train is performed by introducing a variable delay within one of the signals. This experiment uses a very short reference pulse and a more complicated and longer pulse train as inputs. The short reference is scanned in time across the longer signal, and wherever there is overlap a SHG signal is generated. The reference pulse appears to take small samples of the longer input signal, and the output is a SHG signal as a function of delay that appears similar to the pulse train.

The compressed pulse that was intended for the AWG/device array is sent to a polarization controller and polarizer before being sent to the 5nm filter and AWG. The output of the AWG is corrected (due to the ~50m length of fiber within this arm) for chromatic dispersion using dispersion compensated fiber (DCF). Since different wavelengths can travel at different speeds within fibers, a pulse with can appear to be smeared out in time due to these dispersive effects. This depends on the bandwidth of the signal and the length and dispersive properties of the fiber. After dispersion compensation, the optical signal is amplified using an erbium doped fiber amplifier (EDFA) to boost signal strength before cross correlation.

Figure 5.7 shows some DST output waveforms resulting from this setup. First, note for the zero bias case that there are 8 pulses in the output pulse train corresponding to the 8 used array guides. Next, a -15V bias is applied to the third device in the array via probe tip. The corresponding pulse within the pulse train is now suppressed indicating that the spatial profile (device array) has changed. The extinction ratio for pulse shaping is calculated by taking the value of the signal in the "on" state (zero bias) with the background level subtracted and dividing it by the signal in the "off" state (-15V bias) after background removal. The extinction ratio seen here is 34.8 or 15.4dB, and the size of the array device used was 150μm. Other devices within the array can be controlled, showing the flexibility of output waveform control. Figure 5.8(a) shows an output pulse train without any bias on any of the devices. Figures (b-d) show the output waveform while biasing only the second, third and fifth device in the array.

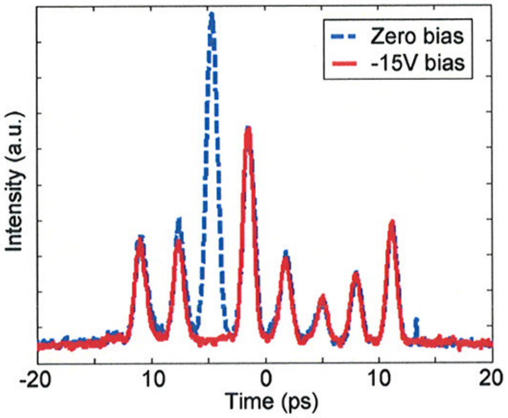

Fig. 5.7. Output pulse trains under different biases.

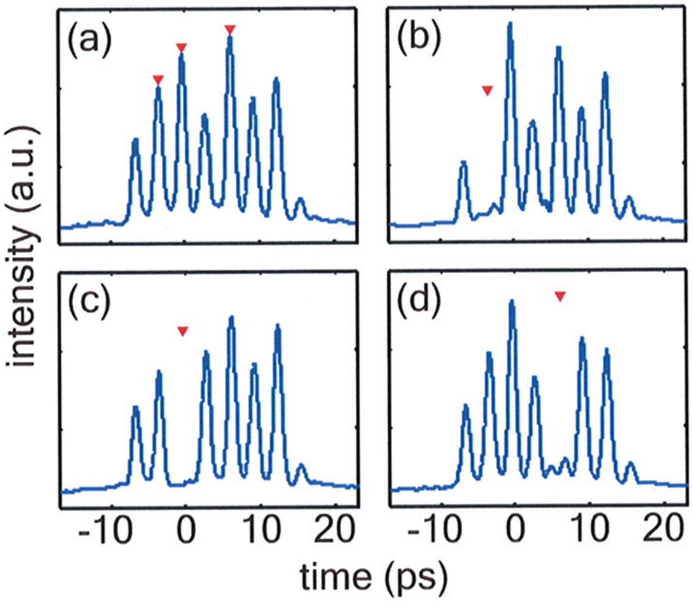

Fig. 5.8. Output pulse trains with different devices under DC bias to show diversity of control.

5.3 Rapid update DST pulse shaping

Simple DST pulse shaping at DC rates was just demonstrated in the previous section. Now, the speed at which the spatial profile is changed is increased by driving a device in the array with an AC signal near the cutoff frequency. Modifications to the previous setup will be needed, and the setup used to demonstrate rapid reconfiguration is shown in figure 5.9. First, the repetition rate of the source laser is much faster than the operating speed of the modulators. The source laser is gated down to the much slower rate of 500MHz by use of an intensity modulator (IM) that will block 19 of 20 of the pulses. A small portion of the high repetition rate optical pulse is converted to an electrical signal by photodiode (PD). This electrical signal is used as a trigger to a bit error rate tester (BERT). A BERT is commonly used to test error rates in communication channels by sending a data pattern into the channel and receiving the data out of the channel. The two are compared to determine the number of errors per unit time. A BERT is not necessary, but its flexibility in constructing

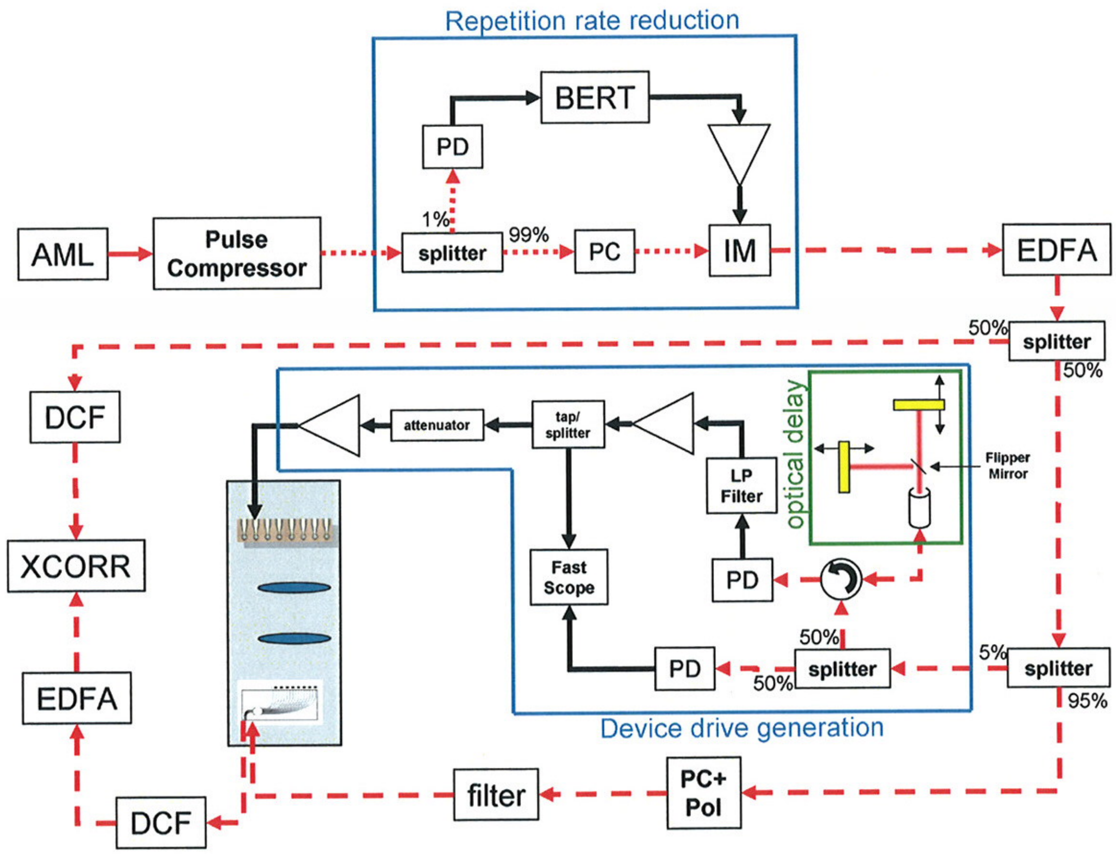

Fig. 5.9. Setup for DST pulse shaping at RF rates. Components: actively mode-locked laser (AML), photodiode (PD), dispersion compensating fiber (DCF), erbium doped fiber amplifier (EDFA), polarization controller (PC), polarizer (Pol), cross correlation (XCORR), intensity modulator (IM), and bit error rate tester (BERT).

various output waveforms allows an easy configuration to output a signal for driving an intensity modulator to reduce the repetition rate. The output of the BERT is amplified in order to properly drive the modulator. After repetition rate reduction, the signal is amplified by an EDFA and half of the signal is dispersion compensated and sent to a cross correlation setup for usage as a reference signal. The other half is split into two arms.

One arm is used to provide a high speed signal that will drive the device. Within the device drive generation portion, power is split into two paths. One path is converted into an electrical signal to trigger a high speed oscilloscope. The other half is sent into a free space variable optical delay through a fiber collimator. This delay is constructed with two mirrors mounted on translation stages and a flipper mirror that selects a path to one of the mirrors. The reflected light returns to the collimator and is fiber coupled before it is sent to a photodiode. This photodiode is responsible for generating the signal which will drive the device. The electrical signal from the PD is low pass filtered to ensure that the signal is smooth and amplified. After amplification, a small portion of the signal is sent to the high speed oscilloscope to monitor the drive waveform. This is done to ensure proper drive levels to the device and that the bias conditions of the intensity modulator used for repetition rate reduction has not changed. The rest of the signal sees a fixed amount of attenuation and amplification to properly drive the device. This device drive portion of the setup is used to generate a signal that can be used to change the reflectivity of the device, but the drive signal also can be delayed with respect to the optical input pulse into the AWG. Having this variable delay allows control over the reflectivity of the modulator as the optical pulse within the pulse shaper illuminates the device.

Light not sent used to generate the drive signal is sent to a polarization controller (PC), polarizer (Pol), and the 5nm filter before being sent to the AWG. The output signal from the AWG is dispersion compensated, amplified via EDFA, and sent to the cross correlation setup for measurement.

The function of the optical delay stage within the device drive generation portion of the setup is to adjust reflectivity of the device when the optical pulse illuminates it. A change in the delay should result in a change in the output optical pulse train from the AWG. This is illustrated in figures 5.10 and 5.11. As the device is being driven (fig. 5.10), a mirror in the optical delay can be moved in one direction to control the reflective state of the device when the pulse hits it. This is noted by the small colored circles on the sine wave. The position and motion of the mirror is chosen to observe the device changing from a high reflective "on" state to a low reflective "off" state. The mirror in the free space delay must be moved 15cm in order to cover the 1ns

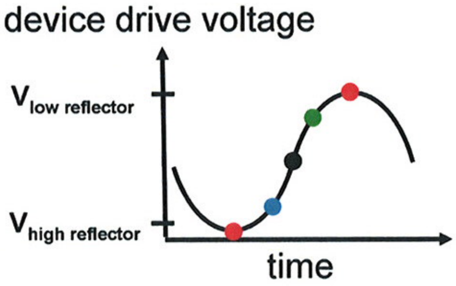

Fig. 5.10. High speed device drive signal.

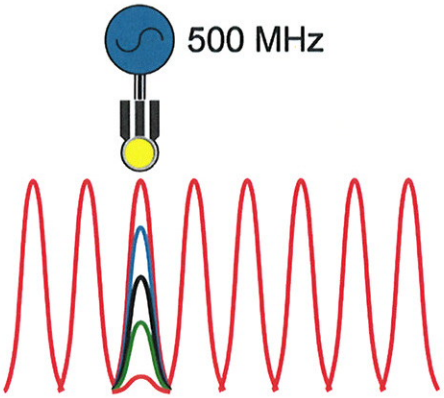

Fig. 5.11. Various AWG output pulse trains due to varying device drive signal.

delay or π phase change of the 500MHz drive signal. The resulting output waveforms (fig. 5.11) show a pulse train that has the pulse which corresponds to the driven device undergo a change from full intensity to low intensity. This concept is proven experimentally and the results are shown in figure 5.12. The above plot was obtained

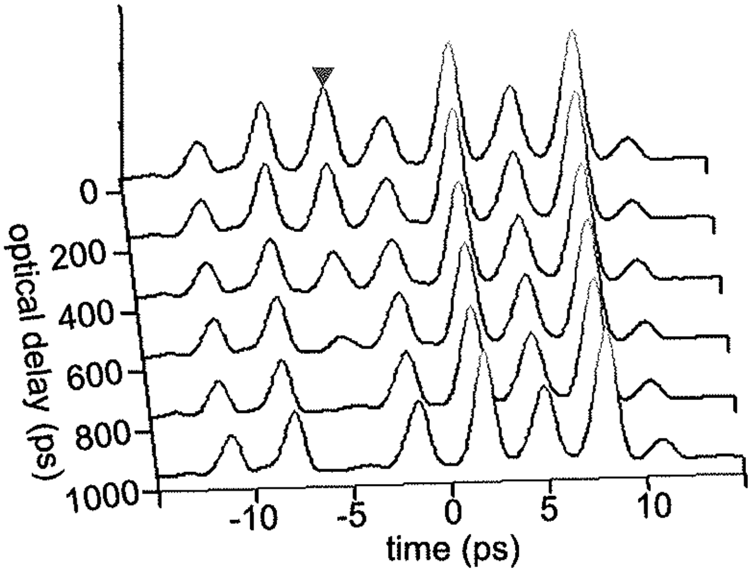

Fig. 5.12. Evolution of output pulse train as RF delay is swept through π range for 500MHz.

while driving the third device in the 150μm array with a -10V bias and +18dBm RF drive power. These drive and bias conditions were chosen to optimize the extinction between the opposing "on/off" states. The pulse indicated with the marker clearly undergoes an evolution from full intensity to suppression.

Focusing on the pulse trains in the "on/off" states will allow the measurement of the high speed extinction ratio. This is calculated by observing one of the pulses in the output waveform in the "on" state and dividing it by the pulse in the "off" state with background removed. Figure 5.13 shows a couple examples of the comparison between states. Figures 5.13 (a) and (b) show the third device in the "on" state and "off" state, while (c,d) show the fifth device under modulation. Both devices were driven with same bias and RF drive conditions mentioned just above. The RF extinction for the third pulse is 11.3dB and 10.4dB for the fifth.

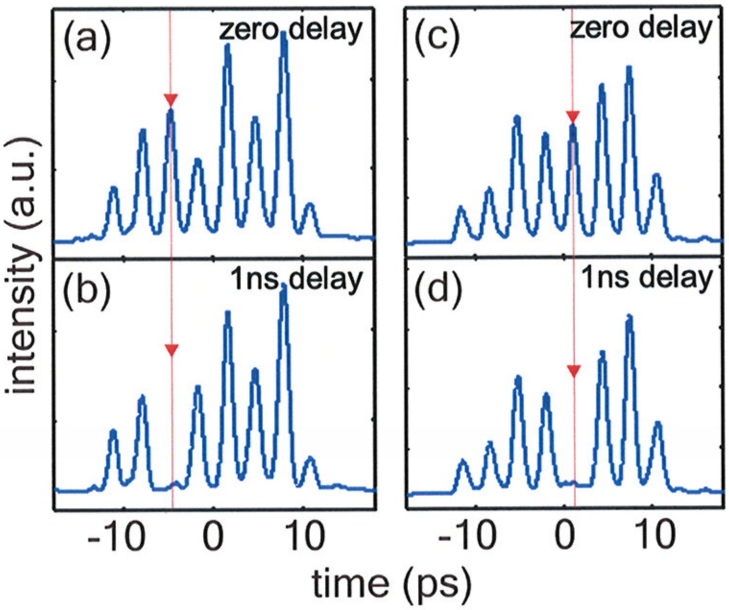

Fig. 5.13. Examples of high speed switching between "on/off" states for two devices.

Higher speed RF testing, similar to figure 5.12, was also conducted for the 150μm array. The modulation frequency of the devices and the repetition rate of the source laser was increased to 1GHz. Again, the delay between the two was varied through the optical delay stage. Figure 5.14 shows the results when the fifth device is driven with +18dBm RF power and a -9V bias. Modulation is readily noted, and this is expected since the cutoff frequency for this device is 922MHz. However, the modulation depth is not quite as large as the 500MHz case. The RF extinction ratio for the 1GHz case is 4.26 (6.3dB). A π delay for a 1GHz signal is 500ps, and the steps in this experiment covered just above that amount with 533ps of delay.

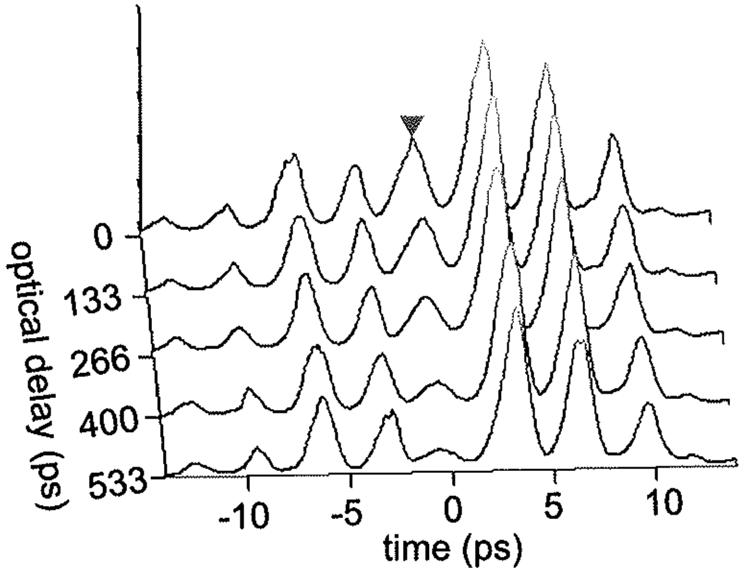

Fig. 5.14. Evolution of output pulse train as RF delay is swept just over a π range for 1GHz.

6. CONCLUSIONS AND FUTURE WORK

6.1 Conslusions

This work has shown a new level of reconfiguration for optical pulse shaping. Using an array of high-speed semiconductor reflection modulators within an integrated direct space-to-time pulse shaper has yielded reconfiguration at 1ns, which is a 30x improvement from the current best. Not only has speed been increased by over an order of magnitude, but waveform quality in terms of the ability to suppress pulses within a pulse train (extinction ratio) is greater than 10dB for both DC and RF operation.

The aforementioned results have allowed advances for reconfigurable pulse shaping, but opportunities for further enhancements exist. Device and system improvements can still deliver faster and more flexible pulse shaping capabilities.

6.2 Device Improvement

6.2.1 New Device Material

One method for advancing performance of the DST shaper is to make modifications to the device. The current device is illuminated through the bottom side of the wafer. The 500μm thickness of the substrate keeps the devices from being placed right at the output face of the waveguide array. If the device was illuminated from the topside, the need for using a telescope would be eliminated. An example material structure is shown in figure 6.1, and similar devices have been implemented for other wavelengths [23, 38]. The current device, seen in figure 6.2, uses a buried semiconductor reflector (~30% reflectivity) as a front mirror and a metallic mirror as a back reflector. The new structure would have a burried high reflectivity of >98% centered

InGaAs	p+ contacting layer	300Å
InAlAs	p-type spacer layer	2750Å
InAlAs	intrinsic layer	750Å
	Quantum wells – 90 periods	
InGaAs	well material	80Å
InAlAs	barrier material	70Å
InAlAs	n-type spacer layer	3000Å
	DBR reflector – 40 periods	
InAlAs	low index material	1203Å
InAlGaAs	high index material	1122Å
InP	substrate	~500um

Fig. 6.1. Material structure for new device.

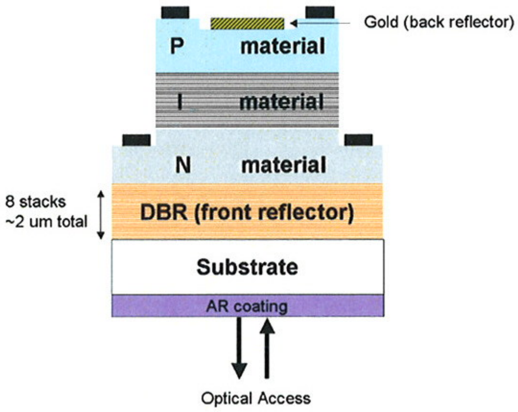

Fig. 6.2. Current device structure with bottom side illumination.

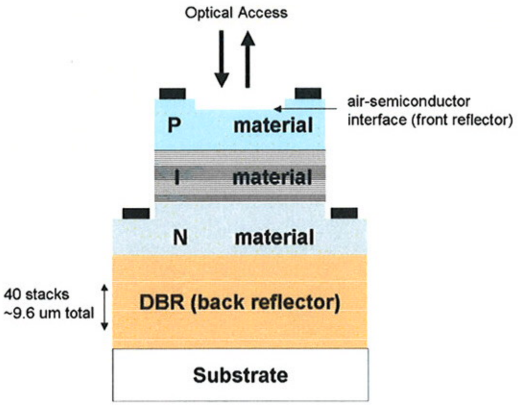

Fig. 6.3. New device structure with top side illumination.

at 1540nm with an ∼80nm bandwidth which acts as the back reflector, see figure 6.3. The front ∼30% reflector would simply be the air to InAlAs interface which provides ∼27% reflectivity. Topside illumination can also reduce the complexity of the device processing since the AR coating is no longer needed to suppress the air to InP reflection from bottom side illumination. The device spacing would have to directly match the output guides, which could pose a spacing issue due to the size of the current devices. However, device size could be reduced dramatically to match the size of the output guide of the AWG which could result in devices with active areas $< 100\mu\text{m}^2$.

The number of quantum wells has also increased from 80 to 90 in order to improve the quality of the "off" state of the device. This would reduce the reflected power in this state, but it comes with a need for an increased applied voltage to maintain the electric field.

6.2.2 Heating

While attempting to perform rapid update DST pulse shaping a heating issue was discovered when driving the drive an array modulator at high speeds. A frequency and power dependent loss was observed. Higher power and frequency drives appeared to reduce the output pulse train intensity from the AWG, and signal would be restored once RF power was terminated. A possible high device resistance caused a heating in the array such that a form of defocussing of the light returned back into the waveguide arrays would occur thus greatly reducing the signal. Figure 6.4 shows an example of the strong signal without RF drive and much weaker signal with RF power. A

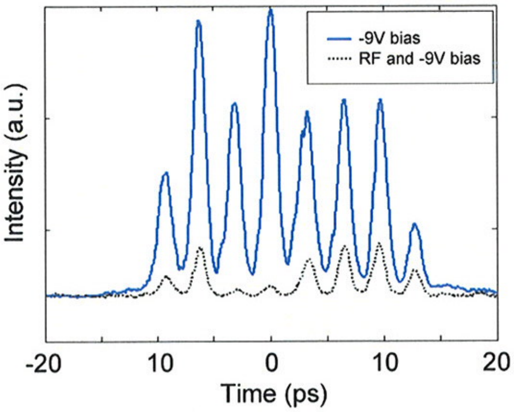

Fig. 6.4. Example of signal degradation when applying an RF signal.

temporary solution was to direct moving air from the topside of the devices (the same side as the RF signal is being applied) to cool the array. This provided a signal strength near to that of just applying DC voltages on a device. A possible source of the high resistance is most likely within the coplanar waveguide (CPW) leads from which the RF+DC bias is applied. The metallic thickness of the CPW is 2000Å of Au. This amount can be more than an order of magnitude smaller than some CPW thicknesses found in literature, and conductor attenuation rises with thinner metal layers [39]. However, if the heating problem stems from high series resistances within the materials, a better heat removal option would be necessary. A metallic heat sink is an option, but will not be easy to implement given the current device operation of bottom side illumination and top side drive. If the new material were to be used to fabricate a top side illuminated device, the bottom side of the wafer could be fixed to a heat sink.

6.2.3 Capacitance

Another form of improving the experiment would be to increase the operating speed of the devices. Currently, cutoff frequencies are ranges of 700MHz to about 2GHz. This arises from the large device capacitance that is formed by the mesa etch described in chapter 3 and shown in red in figure 6.5 (a). This was done to simplify device fabrication by minimizing processing steps. The device capacitance is directly proportional to the area of the PIN diode defined by the mesa etch step, which includes the area under the center conductor of the CPW step. If the device area were to be reduced such that it approached the active area of the device (see figure 6.5 (b) for example), the cutoff frequencies would increase allowing higher speed performance. Table 6.1 shows current devices with their respective areas and cutoff frequencies. A possible reduced area, which does not include the center conductor (as mentioned above), is also included along with estimated cutoff frequencies generated by extending the curve fit from figure 4.4 in chapter 4 to the smaller device areas.

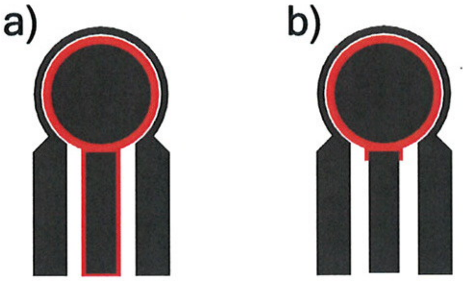

Fig. 6.5. Device area for current device (a) and new device (b).

However, this means that center conductor of the CPW step would not be part of the mesa step and connectivity to the p$^+$ layer would not be straight forward. If the p$^+$ layer and center strip are not at the same levels, they could be connected with an air bridge. An air bridge step would increase the number of processing steps by at least 3 processing steps, increasing the complexity of fabrication and fragility of the wafer piece. Mishandling of the piece could result in crushed air bridges, but covering the wafer piece in photoresist (and patterning specific openings for optical and electrical access) could improve the robustness.

Table 6.1
Current device areas and cutoff frequencies compared with possible reduced area devices and estimated cutoff frequencies.

Device	**Device Area**	**Current Cutoff**	**Reduced Device Area**	**Reduced Est. Cutoff**
D100	47,201μm^2	1.959GHz	19,000μm^2	4.4GHz
D150	64,356μm^2	1.164GHz	38,600μm^2	2.2GHz
A100	71,073μm^2	1.158GHz	14,500μm^2	5.8GHz
A150	83,536μm^2	922MHz	27,000μm^2	3.1GHz
D250	103,686μm^2	703MHz	74,000μm^2	1.1GHz

6.3 Multi-Device Functionality

The ability to modulate a single device within the array demonstrates that rapid update reconfiguration possibilities. However, driving multiple devices at high speed would allow generation of more complicated signals. Currently a single device is driven by an RF probe which makes physical contact with the CPW lines of the devices. The RF probe itself is much larger than the devices and attempting to drive more than one device with these probes is difficult. The ability to drive the devices without using multiple probes is desired an could be accomplished by an external circuit that allows common RF connectors to provide drive signals to each of the devices. The circuit would provide transmission lines that would carry the signals down to the scale of the devices. A possible solution has been partially developed and is shown in figure 6.6. There are two steps within this circuit. There is a transition from features that are on the scale of typical RF connectors down to the limitation of a circuit milling machine which can be used to generate transmission lines. The gap between the minimum milling size and the device size is bridged by a glass slide with metallic transmission lines evaporated on it made possible with photolithography. All of the transmission lines and devices would be connected via wire bonding techniques along

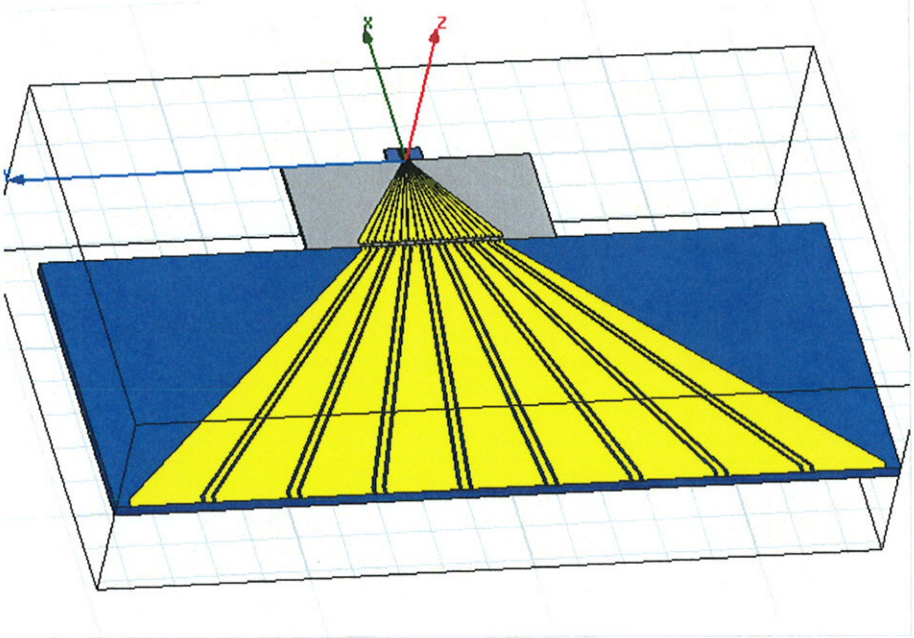

Fig. 6.6. Board with reducing transmission lines to drive more than one device.

with commonly used SubMiniature version A (SMA) connectors on the edge of the board to provide connectivity to RF sources.

LIST OF REFERENCES

LIST OF REFERENCES

[1] A. Weiner, "Femtosecond pulse shaping using spatial light modulators," *Review of Scientific Instruments*, vol. 71, no. 5, pp. 1929 – 1929, 2000.

[2] A. M. Weiner, D. E. Leaird, J. S. Patel, and J. R. Wullert, "Programmable shaping of femtosecond optical pulses by use of a 128-element liquid crystal phase modulator," *IEEE J. Quantum Electron*, vol. QE-28, pp. 908–920, 1992.

[3] D. Leaird and A. Weiner, "Femtosecond optical packet generation by a direct space-to-time pulse shaper," *Opt. Lett.*, vol. 24, no. 12, pp. 853 – 5, 1999.

[4] C. Froehly, B. Colombeau, and M. Vampouille, *Shaping and analysis of picosecond light pulses*, pp. 65 – 153. 1983.

[5] D. E. Leaird and A. M. Weiner, "Femtosecond direct space-to-time pulse shaping in an integrated-optic configuration," *Optics Letters*, vol. 29, pp. 1551–1553, July 2004.

[6] J. P. Heritage, A. M. Weiner, and R. N. Thurston, "Picosecond pulse shaping by spectral phase and amplitude manipulation," *Optics Letters*, vol. 10, pp. 609–611, 1985.

[7] A. M. Weiner, D. E. Leaird, J. S. Patel, and J. R. Wullert, "Programmable femtosecond pulse shaping by using a multielement liquid crystal phase modulator," *Optics Letters*, vol. 15, pp. 326–328, 1990.

[8] J. McKinney, D.-S. Seo, and A. Weiner, "Direct space-to-time pulse shaping at 1.5 um," *IEEE J. Quantum Electron.*, vol. 39, no. 12, pp. 1635 – 44, 2003.

[9] D. E. Leaird and A. M. Weiner, "Femtosecond direct space-to-time pulse shaping," *IEEE J. Quantum Electron*, vol. 37, pp. 494–504, 2001.

[10] S. Yoo, R. Bhat, C. Caneau, J. Gamelin, M. Koza, and T. Lee, "High-speed 1.5-um asymmetric fabry-perot modulators," (Washington, DC, USA), pp. 284 – 5, 1995.

[11] R. Yan, R. Simes, and L. Coldren, "Wide-bandwidth, high-efficiency reflection modulators using an unbalanced fabry-perot structure," *Appl. Phys. Lett.*, vol. 55, no. 19, pp. 1946 – 8, 1989.

[12] A. Krishnan, M. Knapczyk, L. de Peralta, A. Bernussi, and H. Temkin, "Reconfigurable direct space-to-time pulse-shaper based on arrayed waveguide grating multiplexers and digital micromirrors," *IEEE Photonics Technol. Lett.*, vol. 17, no. 9, pp. 1959 – 61, 2005.

[13] A. Tuantranont, T. Lomas, and V. Bright, "Mems micromirrors for optical switching in multi-channel spectrophotometers," vol. 5276, (Perth, WA, Australia), pp. 221 – 229, 2004.

[14] L. Hornbeck, "Combining digital optical mems, cmos and algorithms for unique display solutions," (Washington, DC, United states), pp. 17 – 24, 2007.

[15] G. Nielson, R. O. III, P. Resnick, and O. Spahn, "High-speed mems micromirror switching," (Piscataway, NJ, USA), pp. 548 – 9, 2007.

[16] E. Frumker and Y. Silberberg, "Femtosecond pulse shaping using a two-dimensional liquid-crystal spatial light modulator," *Optics Letters*, vol. 32, no. 11, pp. 1384 – 1386, 2007.

[17] C. Hillegas, J. Tull, D. Goswami, D. Strickland, and W. Warren, "Femtosecond laser pulse shaping by use of microsecond radio-frequency pulses," *Optics Letters*, vol. 19, no. 10, pp. 737 – 739, 1994.

[18] E. Frumker, E. Tal, Y. Silberberg, and D. Majer, "Femtosecond pulse-shape modulation at nanosecond rates," *Opt. Lett.*, vol. 30, no. 20, pp. 2796 – 8, 2005.

[19] C. Fabry and A. Pérot, "Theorie et applications d'une nouvelle methode de spectroscopie interferentielle," *Ann. Chim. Phys.*, vol. 16(7), p. 115, 1899.

[20] J. Verdeyen, *Laser Electronics.* New Jersey: Prentice Hall, fourth ed., 1981.

[21] K.-K. Law, M. Whitehead, J. Merz, and L. Coldren, "Simultaneous achievement of low insertion loss, high contrast and low operating voltage in asymmetric fabry-perot reflection modulator," *Electronics Letters*, vol. 27(20), pp. 1863–1865, September 1991.

[22] P. Zouganeli and G. Parry, "Evaluation of the tolerance of asymmetric fabry-perot modulators with respect to realistic operating conditions," *IEEE Journal of Quantum Electronics*, vol. 31(6), pp. 1140–1151, June 1995.

[23] M. Whitehead, A. Rivers, and G. Parry, "Low-voltage multiple quantum well reflection modulator with on:off ratio >100:1," *Electronics Letters*, vol. 25(15), pp. 984–985, 1989.

[24] A. Beiser, *Concept of Modern Physics.* New York: McGraw-Hill Inc., fourth ed., 1963.

[25] N. Webster, "Reconfigurable direct space-to-time pulse shaping." Purdue University Doctoral Thesis.

[26] D. Miller, "Lecture notes: Semiconductor optical devices 243." Stanford University.

[27] D. Miller, D. Chemla, T. Damen, W. W. A.C. Gossard, T. Wood, and C. Burrus, "Electric field dependence of optical absorption near the band gap of quantum-well structures," *Physical Review B*, vol. 32(2), pp. 1043–1060, July 1985.

[28] S. Mahmoud, "Structure and optical properties of thin titanium films deposited on different substrates," *Fizika*, vol. 19, no. 2, pp. 165 – 73, 1987.

[29] G. Hass and A. Bradford, "Optical properties and oxidation of evaporated titanium films," *Journal of the Optical Society of America*, vol. 47, no. 2, pp. 125 – 129, 1957.

[30] S. Ramo, J. Whinnery, and T. V. Duzer, *Fields and Waves in Communication Electronics*. New York: John Wiley and Sons Inc., fourth ed., 1964.

[31] F. Gervais, *Handbook of optical constants of solids*, vol. 2. San Diego: Academic Press, 1998.

[32] I. Malitson, "Refraction and dispersion of synthetic sapphire," *Journal of the Optical Society of America*, vol. 52, no. 12, pp. 1377 – 1379, 1962.

[33] T. Eriksson, A. Hjortsberg, G. Niklasson, and C. Granqvist, "Infrared optical properties of evaporated alumina films," *Appl. Opt.*, vol. 20, no. 15, pp. 2742 – 6, 1981.

[34] K. Okamoto, "Recent progress of integrated optics planar lightwave circuits," *Opt. Quantum Electron.*, vol. 31, no. 2, pp. 107 – 29, 1999.

[35] D. Leaird, A. Weiner, S. Shen, A. Sugita, S.Kamei, M. Ishii, and K. Okamoto, "High repetition rate femtosecond wdm pulse generation using direct space-to-time pulse shapers and arrayed waveguide gratings," *Optical and Quantum Electronics*, vol. 33, no. 7-10, pp. 811 – 826, 2001.

[36] D. Leaird, A. Weiner, S. Kamei, M. Ishii, A. Sugita, and K. Okamoto, "Generation of flat-topped 500-ghz pulse bursts using loss engineered arrayed waveguide gratings," *IEEE Photonics Technology Letters*, vol. 14, no. 6, pp. 816 – 818, 2002.

[37] A. Weiner, *Ultrafast Optics*. Hoboken, N.J.: Wiley, 2009.

[38] J. Heffernan, M. Maloney, J. Hegarty, and J. Roberts, "Optical switching in an asymmetric fabry-perot with high contrast ratio and very low insertion loss," *Electronics Letters*, vol. 27(8), pp. 659–660, 1991.

[39] A. Rastogi and S. Mishra, "Coplanar waveguide characterization with thick metal coating," *Int. J. Infrared Millim. Waves*, vol. 20, no. 3, pp. 505 – 20, 1999.

APPENDIX

A. DEVICE SIMULATIONS

Computer simulations of the device are accomplished by approaching the device as a transmission line. All of the thin layers of materials can be treated as cascading impedances [30], and knowing the total impedance of the object allows the calculation of the reflection and transmission coefficients. With the coefficients known, the reflectivity and transmissivity can also be determined. First, determining the coefficients from the impedances is important. Looking at a simple transmission line with a simple load, as shown in Figure A.1, the reflection coefficient at the load is shown as

$$\rho = \frac{Z_L - Z_0}{Z_L + Z_0} \tag{A.1}$$

, where Z_L is the load impedance and Z_0 is the characteristic impedance of the line itself. The transmission coefficient at the load is given by

$$\tau = \frac{2Z_L}{Z_L + Z_0} \tag{A.2}$$

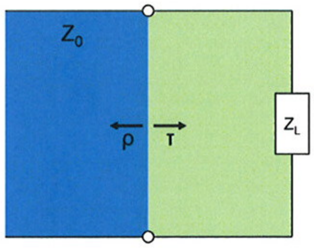

Fig. A.1. Simple transmission line with load impedance

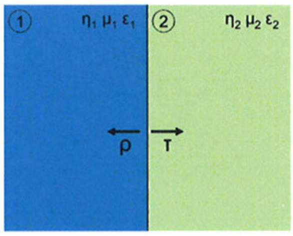

Fig. A.2. Simple interface of two films.

. This simple transmission line can be modified to describe thin films. Instead of having a transmission line and simple load, there are two materials as seen in Figure A.2. Now, the reflection and transmission coefficients at the interface are given by

$$\rho = \frac{\eta_2 - \eta_1}{\eta_2 + \eta_1} \tag{A.3}$$

and

$$\tau = \frac{2\eta_2}{\eta_2 + \eta_1} \tag{A.4}$$

respectively, where η is the characteristic impedance of the material given by

$$\eta = \sqrt{\frac{\mu}{\epsilon}} \tag{A.5}$$

where μ is the material permeability and ϵ is the material permittivity. The permeability and permittivity are further given as $\mu = \mu_r\mu_0$ and $\epsilon = \epsilon_r\epsilon_0$, where μ_r and ϵ_r are the relative permeability and relative permittivity. The permeability and permittivity of free space are μ_0 and ϵ_0, and are constants. These coefficients tell us the relationship between reflected and transmitted electromagnetic fields, but not the power. The reflectivity and transmissivity are given by

$$R = |\rho|^2 \tag{A.6}$$

and

$$T = 1 - |\rho|^2 \tag{A.7}$$

in the case that the material is not absorbing. In order to determine the reflectivity and transmissivity of the device as a whole, the total impedance all the layers must be determined. In order to do this, we use the equation for determining input impedance of a transmission line with a load some distance down the line

$$Z_i = Z_0 \left[\frac{Z_L cos\beta l + jZ_0 sin\beta l}{Z_0 cos\beta l + jZ_L sin\beta l} \right] \tag{A.8}$$

where Z_L is the load impedance, Z_0 is the impedance of the line, l is the distance down the line, and β is the phase constant in the transmission line. An example of

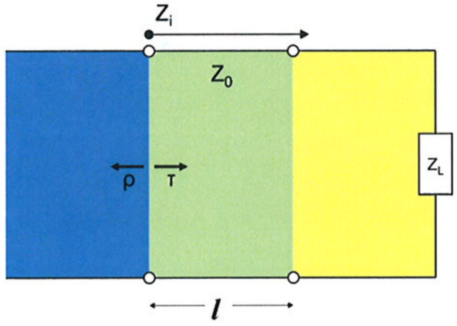

Fig. A.3. Transmission line approach for determining an input impedance

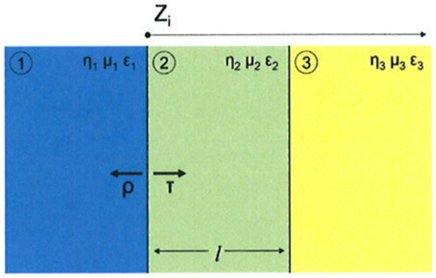

Fig. A.4. Thin film approach for determining an input impedance

this is show in Figure A.3. In the case of two films, the impedance of the films could be determined by

$$Z_i = \eta_2 \left[\frac{\eta_3 coskl + j\eta_2 sinkl}{\eta_2 coskl + j\eta_3 sinkl} \right] \tag{A.9}$$

where η is the impedance of the material, l is the length of the second material, and k is the phase constant for plane waves. Using the above equation, one can reduce materials 2 and 3 into a single load material at the boundary of material 1. This is shown in Figure A.4. This method of determining the impedance for a load material and a film of material can be repeated over and over again until the entire device can be replaced by a total impedance load. Now, with only what appears as an impedance line and load, the reflection and transmission coefficients of the entire device can be solved. Since there is expected absorption in the device, these equations cannot be used as is. The impedance equation changes into a more general form

$$Z_i = Z_0 \left[\frac{Z_L cosh\gamma l + jZ_0 sinh\gamma l}{Z_0 cosh\gamma l + jZ_L sinh\gamma l} \right] \tag{A.10}$$

where the only difference is the use of γ a propagation constant which is defined as

$$\gamma = \alpha + j\beta \tag{A.11}$$

where α is the absorption coefficient of the material of the line, and β is again the phase constant. If $\alpha = 0$, no loss in the material occurs and the general form of the impedance equation becomes equation (A.8). Since there is loss due to the absorption in the device, determining the reflectivity and transmissivity must also change. In the lossless case, the transmissivity is determined by whatever power that is not reflected. Now the absorption causes a need for the transmission to be determined independently of the reflection. In the lossy case, the transmission coefficient is now

$$\tau = \frac{2Z_{tot}}{Z_{tot} + \eta_1} \left(\prod_{k=2}^{n-1} \tau_k \right) \tag{A.12}$$

where Z$_{tot}$ is the total impedance of the device, η_1 is the impedance of the first layer (typically air), and

$$\tau_k = \frac{e^{-\gamma l} \tau_{k,k+1}}{1 + \rho_{k,k+1} e^{-2\gamma l}} \tag{A.13}$$

where

$$\tau_{k,k+1} = \frac{2Z_{L,k+1 \to n}}{\eta_k + Z_{L,k+1 \to n}} \tag{A.14}$$

and

$$\rho_{k,k+1} = \frac{Z_{L,k+1 \to n} - \eta_k}{\eta_k + Z_{L,k+1 \to n}} \tag{A.15}$$

where η_k is the impedance of the kth layer, and $Z_{L,k+1 \to n}$ is the load impedance of all the layers beyond the kth layer consisting of k+1 through n (the total number of layers). The transmission coefficient resembles the equation for the lossless case by the values in front of the product symbol in equation (A.12). The transmissivity and reflectivity is calculated by squaring their respective coefficients, and the absorption is determined by A=1-R-T, which is any power that is not reflected or transmitted.

In order to properly simulate the device, the correct absorption coefficient (α) of the material grown by the wafer vendor must be determined. This was accomplished by performing measurements on a calibration wafer. This calibration wafer had only a substrate, and reduced number (30 instead of 80) of quantum wells (the absorbing material), and large amount of barrier material (InAlAs) before the first well and after the last well. These thick barriers mimic the InAlAs spacers in the full wafer, but were not doped and were for ease of growth. The thicknesses of all the layers in the calibration wafer were given by the vendor in a growth statement, and a simulation of the calibration wafer was calculated using a guess for the absorption coefficient of the well material (InGaAs). The simulation did not match the calibration wafer data, but the simulation was run multiple times iteratively changing the coefficient until the data and simulation matched. This coefficient vector was stored and used in the simulation of the full wafer. The simulation of device under bias is somewhat approached in a similar fashion. The full device under bias without back mirror and without the cavity etch is measured. The calculated absorption from these measurements is fed into the same iterative process to determine the absorption coefficient of the QW material with applied voltage. This method helps simulate the device with bias for the etch process and back mirror application. This method is not the most accurate, since the material complexity is greater than that of the calibration wafer and the simulation contains those extra layers, but it has shown reasonably good agreement with the actual data.

VITA

VITA

Albert Vega completed his undergraduate studies in 2000 by earning a Bachelor of Science in Electrical Engineering from the University of Texas at El Paso. From there, he entered graduate studies in the Electrical Engineering and Computer Engineering department at Purdue University and earned a Master of Science in 2002 with a thesis title “Dispersion Law for Virtually Imaged Phased Array (VIPA) Spectral Dispersers.”